

Narrow bandgap photovoltaic cells

Rui Q. Yang^{a,*}, Wenxiang Huang^{a,b}, Michael B. Santos^b

^a School of Electrical and Computer Engineering, University of Oklahoma, Norman, OK, 73019, USA

^b Homer L. Dodge Department of Physics and Astronomy, University of Oklahoma, Norman, OK, 73019, USA



ARTICLE INFO

Keywords:

Narrow bandgap
Thermophotovoltaics
Semiconductor superlattice
Photovoltaic cells
Quantum wells

ABSTRACT

Research activities and progress in narrow bandgap (<0.5 eV) photovoltaic (PV) cells for applications in thermophotovoltaic (TPV) systems are reviewed and discussed. The device performance and relevant material properties of these narrow bandgap PV cells are summarized and evaluated. Issues and factors that affect narrow bandgap PV device performance are then considered. Narrow bandgap interband cascade PV devices are presented as a promising route to circumvent or alleviate limiting factors in conventional narrow bandgap TPV devices. The operation principle and special features of interband cascade PV devices are described, along with theoretical modeling and experimental results. Finally, a perspective and outlook is provided in conjunction with the review process.

1. Introduction

Photovoltaic (PV) cells made from semiconductors with relatively narrow bandgaps, have been pursued as an attractive device technology to convert radiant energy from a heat source (typically between 1000 and 2000 K) into electricity in a thermophotovoltaic (TPV) system. A typical TPV system [1–5] consists of a heat source, an emitter (also called a radiator), a filter and an array of PV cells. With spectral control and under high intensity illumination, solar TPV systems [6–8] that combine selective emitters with efficient PV cells promise to achieve a high efficiency (e.g., >80%) beyond the Shockley-Quissner limit [9]. Research on narrow bandgap PV cells has been conducted for several decades with the goal of realizing clean, quiet (no moving parts), compact and portable power sources for applications such as waste heat recovery and power beaming.

Most PV cells studied so far for TPV systems use a single *pn* junction based on GaInAsSb/GaSb [10–12] or InGaAsP/InP material systems [1–5,13] with an absorber bandgap (E_g) of 0.5 eV or wider, corresponding to a cutoff wavelength of 2.5 μm or shorter. Radiant photons with energies less than 0.5 eV constitute a large percentage of the radiation from a relatively low-temperature heat source (800–1,500 K), as implied by the plot of Wien's displacement law shown in Fig. 1, but cannot be utilized for energy production. PV cells made from narrow bandgap materials ($E_g < 0.5$ eV) would absorb these low energy photons, with the increased output current density coming at the cost of a reduced output voltage. This trade-off results in an optimal bandgap of

0.2–0.4 eV for heat sources at 1000–2000 K, as indicated by the green curve (triangles) in Fig. 1, with a conversion efficiency exceeding 30% [14,15] even without spectral control. This is relevant for waste-heat recovery applications where the radiant-heat sources are at low temperatures (800–1,500 K) and TPV systems can be made more simply. In fact, the emitter should be kept at the lowest temperature possible in order to avoid overheating of the PV cell. This is important for near-field scenarios [1,16–19] where radiative transfer is enhanced by placing TPV cells at a distance from the emitter that is comparable to (or even much shorter than) the radiation wavelength.

Laser power beaming is another potential application for narrow-bandgap PV cells. For remote energy delivery in various weather conditions, mid-infrared (3–5 μm) light may be the better choice because widely used near-infrared light is subject to higher absorption and scintillation losses. Therefore, narrow bandgap PV cells with good device performance can have important applications and a large impact on power beaming as well as waste heat recovery.

In this paper, we review past and existing efforts in exploring narrow bandgap (<0.5 eV) semiconductor materials and quantum-engineered heterostructures for PV cells, which were initially motivated for TPV applications, but are not limited to this traditional regime. We discuss their device performance and encountered issues, possible innovations, and prospects for future research activities. The paper is arranged as follows. In Section 2, we review conventional narrow bandgap TPV devices, including a discussion of recent research activities such as the near-field TPV configuration. In section 3, we discuss limiting factors

* Corresponding author.

E-mail address: rui.q.yang@ou.edu (R.Q. Yang).

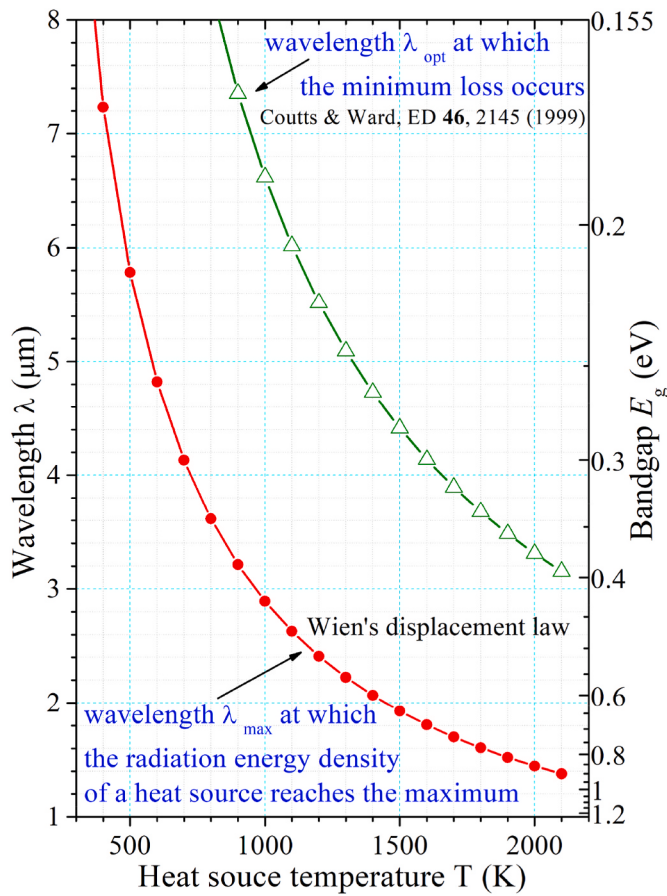


Fig. 1. Radiation wavelengths versus heat source temperature. The minimum bandgap required for absorption is also indicated.

and issues in narrow bandgap PV cells with theoretical perspectives. In section 4, we introduce interband cascade PV cells, then discuss their operation principle, device characteristics and performance. In section 5, we present our outlook and concluding remarks.

2. Narrow bandgap TPV cells

2.1. Far-field TPV cells

In the past, narrow bandgap TPV cells were investigated based on conventional p-n or p-i-n junction structures on InAs [20–25] or InSb substrates [26]. The semiconductor absorber materials were made of InAsSbP [20–22], GaInAsSbP [23], InAs [24,25] or InSb [26] with

bandgaps from 0.23 to 0.48 eV at a cell operating temperature (T_c) of 77–300 K. Under illumination from a heat source such as a quartz-halogen lamp or a blackbody (BB) at a constant temperature (500–950 °C) with a certain input power density (P_{in}), electricity was generated by these narrow bandgap TPV cells with the device performance characterized by measurements of short-circuit current density J_{sc} , open-circuit voltage V_{oc} , bandgap-voltage offset W_{oc} ($=E_g/e-V_{oc}$, where e is the electron charge) [27], voltage efficiency (or voltage factor [3]) η_v ($=eV_{oc}/E_g$), fill factor FF (defined as the ratio $J_m V_m / J_{sc} V_{oc}$, where J_m and V_m are the operating current density and voltage, respectively, when the product $J_m V_m$ is a maximum), power conversion efficiency η , and output power density P_{out} . The device performance data are summarized in Table 1, where most of the values are directly quoted from the cited references. Some values (for quantities not provided in the references) are estimated by us based on the cell size and other given parameters, and therefore may have some variations compared to the actual values.

Most of these TPV cells [20–24] were grown by liquid phase epitaxy (LPE), which permitted the growth of thick (>20 μm) absorber layers [28]. External quantum efficiencies (QE) of over 70% at 2500 nm [20] and 75% at 3000 nm [22] wavelengths were achieved with InAsSbP absorbers at room temperature (RT), resulting in appreciable values of J_{sc} up to 3 A/cm² (~1 A/cm² at $P_{in} = 5.8 \text{ W/cm}^2$). At RT, the open-circuit voltage V_{oc} is low ($\leq 0.17 \text{ V}$). The bandgap-voltage offset W_{oc} ranges from 0.23 to 0.33 V for these TPV cells at RT, which is smaller than a typical value of 0.4 V for solar cells made of wider bandgap (0.67–2.1 eV) semiconductors [27]. However, this does not suggest a better device performance because the ratio of eW_{oc} to E_g is higher in these TPV cells with a small voltage efficiency ($\eta_v \leq 39\%$), resulting in a low power conversion efficiency and output power density (e.g. $\eta < 1.2\%$, $P_{out} < 70 \text{ mW/cm}^2$ at $P_{in} = 5.8 \text{ W/cm}^2$) [22].

The TPV cells [23–25] reported by Lancaster University were grown by LPE [23,24] or metal organic chemical vapor deposition (MOCVD) [25]. The GaInAsSbP absorber in Ref. 23 is about 2 μm thick, the InAs absorber in Ref. 24 is ~6 μm thick, and the intrinsic InAs absorber in Ref. 25 is 10 μm thick. The absorbers in these TPV cells are thinner than in earlier cells [20–22], which may explain the reduced J_{sc} in addition to the somewhat lower illumination power density shown in Table 1. This is partially reflected by the peak external QE of ~60% obtained for TPV cells at 300 K in Ref. [25], which is lower than what was achieved in TPV cells in Refs. [20–22]. Besides the lower FF (<40%), the open-circuit voltages for these InAs TPV cells at 300 K are not higher than 60 mV with η_v less than 20%. This is even lower than that obtained in InAsSbP TPV cells, possibly due partially to the lower illumination power density. When the illumination power density was intensified (with a concentrator in some cases), the V_{oc} and short-circuit current density J_{sc} increased (up to 1.32 and 2.26 A/cm² in Ref. [25]), resulting in higher conversion efficiencies (2.7% in Ref. [24] and 3.6% in Ref. [25]) and increased output power densities (26 and 52 mW/cm² [25]) in the InAs

Table 1
Narrow bandgap TPV cell device performance features.

Absorber material	E_g (eV)	T_c (K)	P_{in} (W/cm ²)	J_{sc} (A/cm ²)	V_{oc} (V)	W_{oc} (V)	η_v (%)	FF	η (%)	P_{out} (mW/cm ²)	Ref
InAsSbP	0.39	RT			0.11	0.28	28				[20]
InAsSbP	0.45–0.48	RT		3	0.15	0.30–0.33	33				[21,22]
InAs _{0.61} Sb _{0.18} P _{0.21}	0.35	294	5.8	1	0.11	0.24	31	<0.7	<1.2	<70	[22]
InAs _{0.84} Sb _{0.03} P _{0.13}	0.44	RT		3	0.17	0.27	39				
GaInAsSbP	0.35	300	0.5	0.29	0.028	0.32	8	0.33	0.54	2.7	[23]
InAs	0.35	300	0.72 ^a	0.89	0.06	0.29	17	0.37	2.7	20	[24]
InAs	0.35	300	0.32	0.23	0.0174	0.33	5	0.25	0.35	1	[25]
			4	2.26	0.052	0.30	15	0.44	1.3	52	
			0.72 ^a	1.32	0.047	0.30	13	0.42	3.6	26	
InSb	0.41	100	0.32	0.16	0.252	0.16	61	0.70	10	28	
InSb	0.23	77		0.03	0.083	0.15	36	0.64	2		[26]

^a Radiation intensity from a BB, P_{in} on TPV cells could be much higher due to the use of a concentrator.

TPV cells.

Overall, the device performance of narrow bandgap TPV cells at RT is well below the theoretically expected level and is not comparable to current TPV cells with wider bandgaps (>0.5 eV). One primary reason is the high dark current density that results from the very high thermally-generated carrier concentration in narrow bandgap materials at room temperature. To alleviate this issue, InAs TPV cells were investigated at low temperatures [25]. At 100 K, J_{sc} was reduced because the bandgap of InAs increased to 0.41 eV, but V_{oc} was significantly increased to 0.252 V with η_v of 61% and FF of 70%. As such, the power conversion efficiency was raised to 10% even with a low P_{in} (0.32 W/cm 2). Recently, Cakiroglu et al. investigated InSb TPV cells with an unintentionally doped 2.5-μm-thick n-type InSb absorption layer grown by molecular beam epitaxy (MBE) [26]. With a bandgap of 0.23 eV at 77 K and under illumination from a thermal emitter at 1248 K, V_{oc} was only 83 mV with η_v of 36% and FF was 64% with a P_{out} of 2 mW/cm 2 . This type of TPV cells may have potential applications in deep space where the ambient temperature is well below 77 K.

More recently, a Bi₂Te₃/Si heterostructure with a 310-nm Bi₂Te₃ thin film as an absorber layer was explored for TPV applications [29]. The Bi₂Te₃ thin film is polycrystalline and has a bandgap of 0.15–0.17 eV. Under illumination from a BB radiation source at temperatures from 300 to 480 K, a photo-response was observed at wavelengths up to 8.2 μm, consistent with the bandgap of the Bi₂Te₃ thin film. Nevertheless, the maximum V_{oc} was only 1.76 mV with J_{sc} of 105 μA/cm 2 and FF of 25.6%, resulting in a very low power conversion efficiency (<0.0005%). Hence, at its current stage, the Bi₂Te₃/Si heterostructure would not have a practical application as a TPV device for generating electricity.

2.2. Near-field TPV cells

The energy transfer between the heat source and the TPV cell can be significantly enhanced by placing the TPV cell at a nanoscale distance from the source. Consequently, PV cells in such a near-field TPV system can have improved device performance in terms of increased output power and open-circuit voltage. Two InAsSb narrow bandgap photodiodes ($E_g \sim 0.345$ eV and 0.303 eV at RT) were explored in a near-field TPV system [18]. Under illumination by a heat source at a range of temperatures (525–655 K) at a distance varied from 12 μm to 60 nm from the PV cell, a significant increase in the short-circuit current, open-circuit voltage, and output power was observed from the TPV cells when the distance was made shorter than 300 nm. However, the attained maximum V_{oc} was less than 1.8 mV with a maximum output power of ~30 nW, resulting in a conversion efficiency of less than 0.015%. Also, the device performance of the PV cell with a 0.303 eV bandgap was worse than that of the PV cell with a bandgap of 0.345 eV, indicating more challenges and difficulties with the narrower bandgap materials.

More recently, Lucchesi et al. explored InSb TPV cells ($E_g \sim 0.23$ eV) in a near-field configuration with the cells cooled down to 77 K [19]. With a hot source (730 K) at a distance of a few μm to 80 nm to the TPV cell, an open-circuit voltage of 127–138 mV with η_v of 55%–60%, FF of 69–75%, output power density of 0.75 W/cm 2 , and power conversion efficiency η of 14% were obtained. This demonstration is remarkable for a narrow bandgap PV cell in a near-field TPV configuration even though it was achieved at 77 K. However, it remains unanswered whether a narrow bandgap TPV cell can be operated at RT in a near-field TPV system with appreciable device performance.

3. Limiting factors and issues in narrow bandgap TPV cells

Research on TPV cells has so far only yielded efficiencies [1–5,30] that are significantly lower than predicted theoretically, with only a few reports on cells with narrow bandgaps ($E_g < 0.5$ eV). As the bandgap is made narrower, several material properties become more disadvantageous for TPV applications, including a high intrinsic carrier

concentration (that exponentially increases with the decrease of the bandgap), a relatively low absorption coefficient (α), and a short diffusion length (L). The material quality is also not as high as for wider bandgap materials such as GaAs. These material properties lead to devices with a higher dark current density and a lower open-circuit voltage. For example, the bulk forms of InAs and InSb (intrinsic or lightly doped) have α values between 1000 and 3000 cm $^{-1}$ for photons with energies near the bandgap. Although L can be several microns without illumination, it can be reduced substantially when a high concentration of excess carriers is created under intense illumination. Engineered type-II (T2) InAs/GaSb superlattices (SLs) with cutoff wavelengths between 4.3 and 5.2 μm, have α values between 2000 and 3000 cm $^{-1}$ for photons with energies near the bandgap. L is estimated to be about 1 μm at room temperature, based on the temperature dependence and bias sensitivity of the responsivity measured for infrared detectors made from T2 InAs/GaSb SLs [31–33].

Fig. 2 (a) shows the substantial impact that a small α and limited L have on TPV device performance. The collection efficiency (η_c) of photo-generated carriers and the external QE (η_q) are calculated as functions of normalized absorber thickness (d/L) [34], using standard theories for p-n junction and barrier photodetector structures [35–37] without considering surface reflection of the light. The calculations indicate that a high η_c (>90%) can be obtained only when the absorber is thinner than the diffusion length. However, the absorber must be thicker than $1/\alpha$ in order to achieve significant absorption of radiant photons or thicker than L when $\alpha L < 1$. Note that η_q does not increase much further with increasing absorber thickness (d) beyond $d \approx L$ because some photo-generated carriers recombine before being collected. Therefore, the collection efficiency η_c , which equals $\eta_q/[1-\exp(-\alpha d)]$ and is the ratio of collected carriers to absorbed photons, is reduced as d is increased or αL is decreased. Also, from Fig. 2 (a) one can see that η_q reaches a maximum at a finite absorber thickness when $\alpha L > 1$, because the collection probability of photo-generated carriers is reduced as the absorber thickness is increased.

A smaller η_q reduces the open-circuit voltage V_{oc} according to [38].

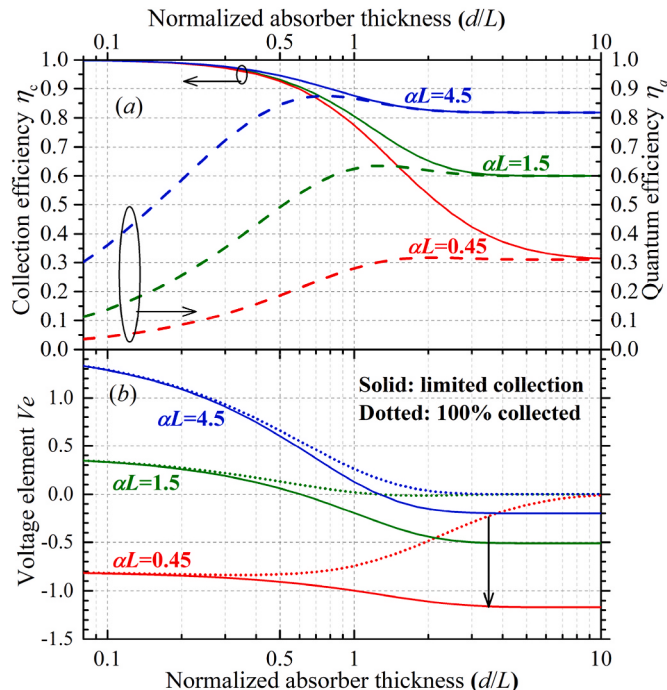


Fig. 2. (a) Calculated collection and quantum efficiencies, (b) voltage element (V_e) as a function of normalized absorber thickness d/L . The voltage element initially decreases with increasing d/L due to the nearly linear increase of dark current density when d/L is small.

$$eV_{oc} = k_b T_c \ln\{\eta_q \Phi_0 / [g_{th} L \tanh(d/L)]\} = k_b T_c \{Ve + \ln[\Phi_0 / (g_{th} L)]\}, \quad (1)$$

where $Ve = \ln[\eta_q / \tanh(d/L)]$ is a voltage element that depends on η_q , k_b is Boltzmann's constant, Φ_0 is the photon flux, and g_{th} is the thermal generation rate. Fig. 2 (b) illustrates this behavior by showing how the voltage element Ve depends on d/L assuming a perfect η_c (dotted curves) or a finite η_c (solid curves) calculated using the η_q in Fig. 2 (a). The value for Ve is reduced noticeably for a finite η_c especially when $\alpha L < 1$ and $d > L$. For example, the arrow in Fig. 2(b) indicates that Ve is reduced by 0.92 when $d = 3.5L$ and αL is reduced from 4.5 to 0.45, resulting in a reduction of V_{oc} by 24 mV at 300 K according to Eq. (1). Hence, the conversion of radiant photons into electricity in a conventional single-absorber TPV structure is substantially limited by the finite diffusion length, especially in narrow bandgap semiconductors where αL is typically less than one. The calculated results in Fig. 2 are based on carrier transport by diffusion. Although a real situation may be more complicated, the qualitative picture revealed in Fig. 2 should be correct.

The theoretical limit for the conversion efficiency of a conventional TPV cell with an InAs/GaSb T2SL absorber, as an example of a narrow bandgap absorber, was investigated for several different scenarios under monochromatic illumination [39]. Considering a bandgap of 0.29 eV and using realistic material parameters (e.g. $L = 1.5 \mu\text{m}$ and carrier lifetime $\tau = 20 \text{ ns}$) extracted from studies of InAs/GaSb infrared detectors [31–33,40], the conversion efficiency (η) and FF are calculated for single-absorber devices illuminated at 50 W/cm^2 , as shown in Fig. 3 for $\alpha L = 0.45$ (realistic case with $\tau = 20 \text{ ns}$), 1.5 ($\tau = 200 \text{ ns}$), 4.5 (radiative limit) and the ultimate limit by setting $V_{oc} = E_g/e$ [39]. The

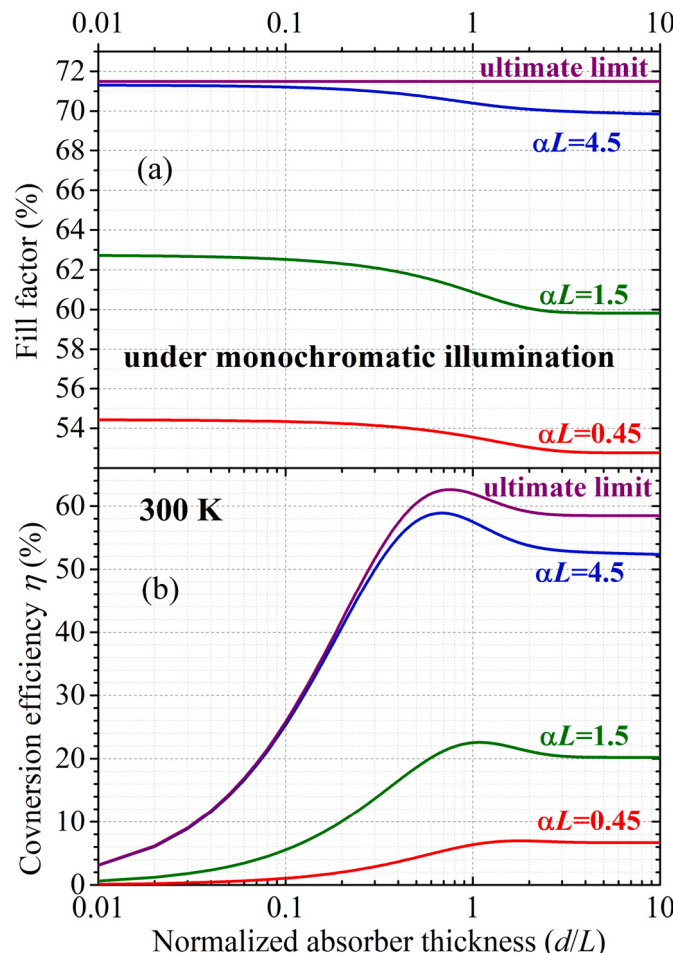


Fig. 3. Calculated (a) FF and (b) η vs normalized absorber thickness (d/L) for several values of αL where $P_{in} = 50 \text{ W/cm}^2$ except for the ultimate limit.

maximum value for η is about 59% in the radiative limit, which is slightly below 63% for the ultimate limit. The very different carrier lifetime for the actual device ($\alpha L = 0.45$) explains its significantly lower η of less than 7%, reflecting a vast potential for enhancement through improved material quality. The conversion efficiency is substantially constrained by the low V_{oc} ($< 0.13 \text{ V}$ [39] with $\eta_v < 45\%$) and low FF ($< 55\%$) that arise from a high saturation current density J_0 (on the order of 0.1 A/cm^2 [39]) with a short carrier lifetime (20 ns). The η will be possibly enhanced to 23% if the carrier lifetime can be increased by an order of magnitude ($\alpha L = 1.5$). These results unambiguously show that the short carrier lifetime is a major issue in narrow-bandgap TPV devices and an appreciable improvement in efficiency will require increasing the carrier lifetime.

Actual devices are also limited by the relatively low QE associated with a small αL , which is less than 32% for an αL value of 0.45. Fig. 3 shows that the dependence of the conversion efficiency η on the absorber thickness follows a similar behavior as η_q versus d/L (Fig. 2). The value of η is maximized at a certain absorber thickness, then decreases slightly before reaching a plateau as d is further increased. The maximum η is reached when d/L equals 1.8, 1.1 and 0.7 for an αL value of 0.45, 1.5 and 4.5, respectively. These values of d/L are somewhat thinner than the d/L values (2.0, 1.3, 0.8 for αL value of 0.45, 1.5, 4.5, respectively) for maximum QE. This is explained by the decrease in V_{oc} and FF as d/L is increased.

In practice, the incident power density in a regular TPV configuration would not reach 50 W/cm^2 , although such a high power density is possible with a concentrator or through illumination from a laser. Reducing the P_{in} , for example from 50 W/cm^2 to 25 W/cm^2 , would result in a decrease of η and FF for each value of αL , but not by very much. Explicitly, the η (FF) decreases from 7% (53%), 23% (61%) and 59% (71%) to 6% (50%), 19% (58%) and 54% (69%) for $\alpha L = 0.45, 1.5$ and 4.5, respectively [39]. The reduction of η and FF is modest because the V_{oc} only decreases by a small amount, despite the 50% reduction of the J_{sc} . Hence, the insights gained from modeling using an incident power density of 50 W/cm^2 can also be applied to situations where the P_{in} is lower.

The device performance of TPV cells strongly depends on the bandgap. An enormous reduction of the dark saturation current density J_0 is expected with an increase of E_g because the thermal generation rate is proportional to $\exp(-E_g/k_b T_c)$. This results in significant rises in FF, voltage efficiency η_v and conversion efficiency η . For example in Ref. 39, the conversion efficiency η for $\alpha L = 0.45$ is raised from 3% to 12% when the bandgap is increased from 0.2 eV to 0.4 eV. However, the η_q at the optimal absorber thickness was almost independent of bandgap for each value of αL . The maximum η_q is limited by the value of αL , while insensitive to E_g . The small value of αL in narrow bandgap materials limits the power conversion efficiency (e.g., $\eta < 15\%$) observed in single junction TPV cells. The next section on the multi-stage interband cascade architecture describes how this problem can be solved or alleviated.

4. Interband cascade (IC) PV devices

4.1. Operation principle and advantages

Quantum-engineered ICPV devices originate from mid-infrared IC lasers (ICLs) [41,42], which have been advanced remarkably in recent years, and nowadays are routinely produced and commercially available [43–45]. ICPV devices are based on III-V quantum well (QW) and SL heterostructures made from InAs, GaSb, AlSb and their alloys [46–48], which are all nearly lattice matched to each other. ICPV devices take advantage of the type-II broken-gap alignment at the InAs/GaSb interface, which enables smooth interband tunneling between cascade stages as shown in Fig. 4 and the bandgap of an InAs/GaSb SL to be even smaller than that of GaSb or InAs. Theoretical calculations indicate that the bandgap can be as small as 75 meV, as experimentally confirmed by

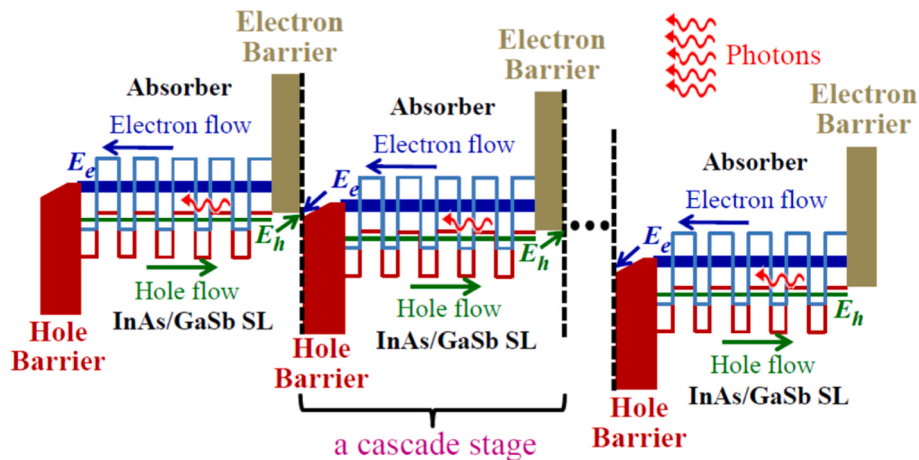


Fig. 4. Schematic illustration of an ICPV structure with multiple interband cascade stages. E_h and E_e denote the energy for hole (olive) and electron (blue) in the valence and conduction bands, respectively. The bandgap (E_g) of the SL is determined by the energy difference ($E_e - E_h$). (For interpretation of the references to color in this figure legend, the reader is referred to the Web version of this article.)

a cutoff wavelength longer than 16 μm for a type-II SL photodetectors [49] and electroluminescence at wavelengths longer than 15 μm from an interband cascade light emitting device at RT [50]. Incorporating an additional Al(In)Sb alloy can make the bandgap as large as 620 meV, which corresponds to a cutoff wavelength of 2 μm .

Fig. 4 schematically shows a quantum-engineered multi-stage ICPV structure, where interband tunnel heterojunctions connect multiple InAs/GaSb SL absorbers in series [51–59]. The bandgaps of individual absorbers in separate stages can be designed for absorbing photons in the same or different spectral bands. The hole and electron barriers block their namesake carriers. In other words, only holes are allowed in the electron barrier, while only electrons are allowed in the hole barrier. When electron-hole pairs are created by photoexcitation in one stage, the electrons and holes diffuse toward opposite edges of the stage. This is in contrast to a *p-i-n* PV device, where the photoexcited electrons and holes are separated by the electric field in the intrinsic region.

Because the interface between the hole and electron barriers is like semi-metallic with a type-II heterostructure, holes from one stage can recombine with electrons from the next stage. Alternatively, one could equivalently describe the situation as holes from the valence band in one absorber tunneling into the conduction band of the next absorber. These tunnel junctions connect the discrete absorbers in series, as in a multi-junction tandem solar cell, but with the necessary band profile created without conventional *p-n* junctions. Eliminating the conventional depletion region in *p-n* junctions also provides the advantage of suppressing the Shockley-Read-Hall (SRH) generation current, resulting in a reduced saturation dark current density.

Fig. 5 shows a calculated band profile for the interface region between two InAs/GaSb SL absorbers. The hole and electron barriers are composed of InAs/Al(In)Sb QWs and AlSb/GaSb QWs, respectively. Photo-generated carriers will be collected in a very short time scale, before they disappear via various recombination and scattering

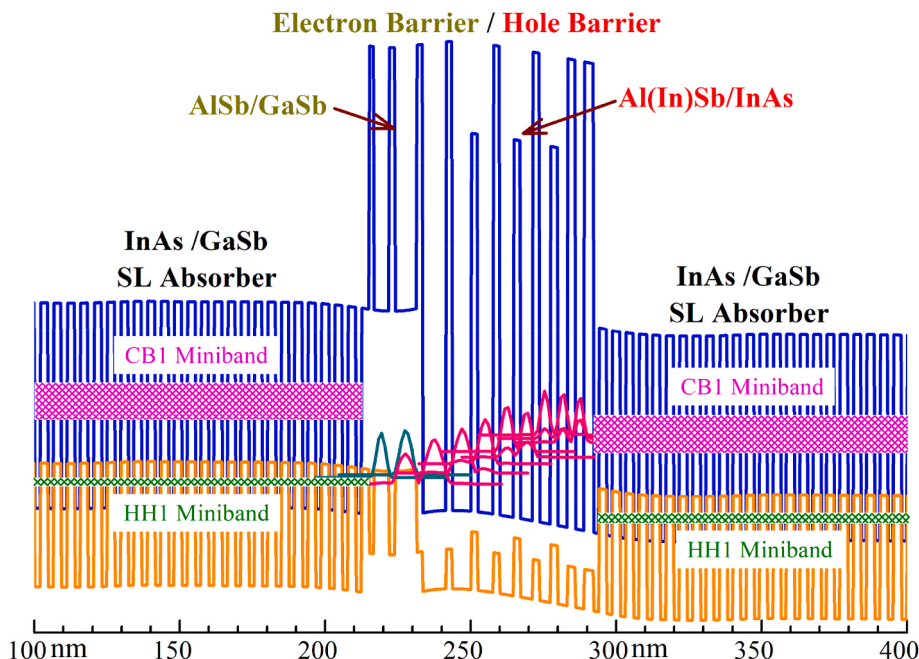


Fig. 5. Detailed layer structure and band diagram for a quantum engineered ICPV structure. The olive and magenta crosshatched rectangles in the absorbers represent the hole and electron minibands. The wavefunctions of ground state energy levels for the QWs of the barrier regions are shown in green for hole states and in pink for electron states. (For interpretation of the references to color in this figure legend, the reader is referred to the Web version of this article.)

mechanisms, potentially resulting in nearly 100% collection efficiency. Several distinct features in ICPV structures enable the carriers to move fast and reach a collection point that is at most only a single cascade stage distance away, a distance designed to be shorter than the diffusion length. When electrons and holes are photo-generated in the minibands of individual absorbers, they will diffuse in opposite directions due to asymmetric band profiles, and then recombine with carriers from adjacent absorbers at the semi-metallic interface (InAs/AlSb/GaSb) between the electron and hole barriers. Hence, these interfaces together with two contact layers at the two ends of the ICPV structures act as equivalent collection points of photo-generated carriers, and they effectively travel over only a single stage before they recombine. The collection efficiency is nearly 100% because the interband recombination time (~ 1 ns in a typical situation or longer in very good materials) via various scattering mechanisms is much longer than the transit time for these carriers to travel across a single stage.

The short transit time (e.g., <0.5 ns) can be ensured by the design of multi-stage ICPV structures. Specifically, the hole barrier is constructed with digitally-graded multiple QWs to form an energy ladder with discrete subband steps in the conduction band, as shown by the dark blue-color in Fig. 5. The right end of the energy ladder is next to the adjoining absorber's conduction band, while the left end is next to the electron barrier's valence band. Or effectively, the conduction band-edge profile in the hole barrier acts as a slide for electrons as shown in Fig. 4, which plays a role equivalent to an internal electric field. Nearly 100% of the photo-excited electrons in the absorber are transferred to the bottom of the energy ladder (or the slide) because the intersubband relaxation that helps electrons move down the ladder (or be swept down the slide) is much faster (on the order of picoseconds) than the interband recombination (on the order of nanoseconds).

Once electrons reach the bottom of the energy ladder, they will quickly tunnel into the valence band of the electron barrier in the adjacent stage. The interband tunneling time in the type-II heterostructure is on the order of picoseconds or shorter with a thin barrier [60,61]. This tunneling mechanism enables the quick and efficient removal of electrons and holes after photoexcitation. By incorporating absorbers with different bandgaps, the discrete absorber architecture can be used for spectral splitting. When the ICPV structure is illuminated, the photo-voltages from the individual absorber stages add together to create a high overall open-circuit voltage, similar to multi-junction solar cells, while the photocurrent is reduced with shortened individual absorbers.

Even when each absorber has the same bandgap, a multi-stage IC structure is still beneficial because the photo-generated carriers can be collected more efficiently, resulting in enhanced power conversion efficiency compared to the conventional single-stage PV cell. However, it is very challenging to achieve current matching in a real device with many stages, especially under illumination from a broadband light source. The challenges are relaxed somewhat when illumination is from a monochromatic light source. Fig. 6 shows the calculated conversion efficiency as a function of the number of cascade stages N_c and αL for an ICPV with a bandgap of 0.29 eV for each T2SL absorber [39] for such cases. For αL values of 4.5, 1.5 and 0.45, the conversion efficiency η is raised from 59%, 23% and 7% in a single-absorber configuration to 68%, 33% and 17% in a multi-stage ICPV structure, respectively. The η increased by 9–10% points for all values of αL . The relative change in η is larger when the N_c is increased for a smaller αL . For instance, for $\alpha L = 0.45$, the efficiency for multi-stage devices is more than double that for single-stage devices.

This can be understood by looking at the particle conversion efficiency η_{part} , which is defined as the sum of the percentage of collected photo-generated carriers in each stage [37,38] and equals $N_c \eta_q$ for current-matched ICPV structures. When the incident light intensity is high, the ratio of the open-circuit voltage $V_{oc}(N_c)$ for the ICPV device with N_c cascade stages to $V_{oc}(1)$ for a single-stage PV device can be approximated as $V_{oc}(N_c)/V_{oc}(1) \approx N_c$, and the fill factor for devices with

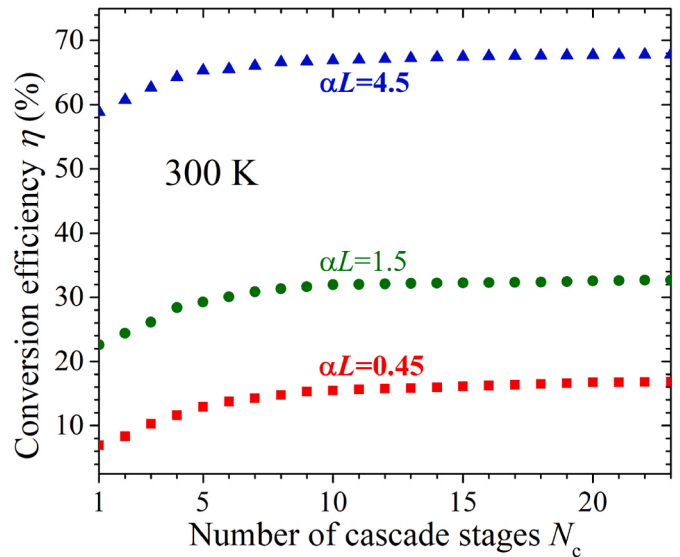


Fig. 6. Calculated power conversion efficiency for optimized multi-stage devices (with a $E_g = 0.29$ eV for the InAs/GaSb SL absorbers) as a function of N_c and under monochromatic illumination at a wavelength matched to the bandgap, where $P_{in} = 50$ W/cm².

different numbers of stages is nearly the same, i.e. $FF(N_c)/FF(1) \approx 1$ [38, 39]. Then the efficiency enhancement in a multi-stage structure $\eta(N_c)/\eta(1)$ can be approximately expressed as [38,39]:

$$\frac{\eta(N_c)}{\eta(1)} = \frac{\eta_q(N_c)}{\eta_q(1)} \cdot \frac{V_{oc}(N_c)}{V_{oc}(1)} \cdot \frac{FF(N_c)}{FF(1)} \approx \frac{N_c \cdot \eta_q(N_c)}{\eta_q(1)} = \frac{\eta_{part}(N_c)}{\eta_q(1)} \quad (2)$$

According to Eq. (2), the conversion efficiency of a photocurrent-matched IC structure is enhanced essentially due to its increased particle conversion efficiency η_{part} . Increasing N_c while making the individual absorbers proportionally thinner, will reduce $\eta_q(N_c)$ but increase η_{part} . Therefore, the conversion efficiency enhancement increases with N_c as shown in Fig. 6. From Fig. 2, $\eta(N_c)/\eta(1)$ can be significant for small αL because $\eta_q(1)$ is low. For large αL , $\eta(N_c)/\eta(1)$ is less significant because $\eta_q(1)$ is relatively high, yet it still exceeds unit with nearly the same increase in $\eta(N_c)$ as that for a small αL . These dependences show how multi-stage ICPV devices enhance the η through an increased η_{part} . The shortened individual absorbers more efficiently collect the photo-generated carriers, which would otherwise be lost to recombination with a thick absorber.

Additionally, the higher operating voltage of the multi-stage IC architecture enables the operating current density to be lowered without sacrificing power conversion efficiency. Lowering the current density mitigates the power lost through series resistance. Another advantage is the design flexibility offered by quantum engineering. For example, neighboring stages in a conventional tandem solar cell are connected by a heavily-doped Esaki tunnel junction, which has the detrimental side effects of free carrier absorption and additional series resistance. In contrast, a multi-stage ICPV device relies on a natural type-II broken-gap junction, which is undoped and has much less resistance than an Esaki tunnel junction. This provides the flexibility to alleviate challenges and optimize the power conversion efficiency by adjusting the number of individual absorbers, in addition to the absorber thickness in each stage. Furthermore, an entire ICPV structure with multiple stages and a range of absorber bandgaps can be grown by MBE on an (001) InAs or GaSb substrate. An ICPV device can efficiently generate current from photons across a very wide infrared spectrum, including wavelengths longer than 10 μm. With these features, quantum engineered ICPV heterostructures offer a very promising option for achieving high performance in TPV systems at RT and above.

4.2. Experimental investigations

4.2.1. Illumination from a blackbody (BB) radiation source

In 2010, the initial study of IC structures for TPV devices [51] was carried out using an IC infrared photodetector structure (ICIP) with 7 identical InAs/GaSb SL absorbers [62] and an ICL device having 11 discrete W-shape QWs [63,64]. Shortly afterward, a similar IC structure having 7 identical InAs/GaSb SL absorbers with a somewhat wider bandgap (0.31 eV at 80 K) was studied for TPV applications [52]. Under illumination by a standard BB radiation source at various temperatures (T_B), the ICPV devices exhibited high open-circuit voltages ($>E_g/e$) as expected. For example, one device from the ICIP wafer ($E_g = 0.24$ eV at 80 K) showed an open-circuit voltage of 1.17 V with a voltage efficiency η_v of 70% ($=eV_{oc}/N_cE_g$, where the N_c factor normalizes for ICPV devices with different numbers of cascade stages for a fair comparison) and W_{oc} of 0.073 V ($=E_g/e \cdot V_{oc}/N_c$). Even with a narrow bandgap of 0.17 eV, an ICL device exhibited a V_{oc} of 0.52 V. The observed high V_{oc} demonstrated that multiple stages were operating in series and provided an initial proof of concept for ICPV devices. A more complete set of device performance characteristics for representative ICPV cells is presented in Table 2. Most of the data are directly quoted from the cited references, but some data (which were not provided in the references) are estimated based on available records.

As shown in Table 2, although the bandgap-voltage offset ($\propto T_c$ [27]), voltage efficiency and FF are reasonable (e.g. FF~66%, $W_{oc} \approx 0.083$ V, $\eta_v \approx 66\%-75\%$ for ICPV devices with $E_g \geq 0.24$ eV) at 80 K, the obtained power conversion efficiency is somewhat low (<5%). One reason is that the total absorber thickness of about 1.1 μm or less may only be enough to absorb and collect 50% or less of the incident photons, as discussed in Ref. [52]. Also, photocurrents between stages are not matched since the individual absorbers in every device were designed to have the same thickness. Other factors include losses due to a finite transmission through the cryostat window, and substantial reflection from the semiconductor surface and metal contacts. Additionally, the device temperature was actually higher than the nominal value of 80 K due to heating from the BB source when placed close to the device, as evidenced by the reduction of V_{oc} from 1.68 V (recorded initially) to 1.63 V in the steady state condition reported in Ref. 52. Hence, the power conversion efficiency for ICPV devices can be higher than 10% at 80 K with improvements such as increasing the total absorber thickness, designing individual absorbers with varying thicknesses for current matching, and depositing an antireflection coating.

Generally, the device performance improves with an increase of the bandgap and a higher illumination intensity. However, despite having a higher V_{oc} and η_v (e.g. 75%), the ICPV device with $E_g = 0.31$ eV (at 80 K) had a FF (45%-46%) that was lower than that for the device with $E_g = 0.24$ eV (at 80 K). This is not fully understood and might be related to possible side-wall current leakage at a relatively high forward bias voltage due to imperfect device fabrication. Nevertheless, the device with $E_g = 0.31$ eV exhibited the higher power conversion efficiency under illumination of similar intensity. When operating at 300 K under illumination from the same BB source, the obtained open-circuit voltage

was reduced dramatically from 1.47 V to 5.7 mV with W_{oc} of 0.259 V being nearly equal to the bandgap (E_g/e). This was because the saturation dark current density at 300 K was significantly higher than the photocurrent density generated by the weak radiation from the BB source, resulting in a negligible electrical power density (<0.003 mW/cm²). The high value of W_{oc} also suggests a relatively short carrier lifetime associated with non-radiative processes [27] in type-II InAs-/GaSb SL absorbers. Hence, to study these narrow bandgap PV devices at RT or above, it is desirable to either increase the illumination intensity or reduce the saturation dark current density. Later, ICPV devices were investigated at RT using mid-infrared ICLs at various wavelengths [34, 53-59], which corresponded to selective emitters for a TPV system, but with high light intensities. Although the ICL illumination is beyond the conventional TPV context with broadband radiation sources, it is helpful to understand and investigate how the ICPV devices would operate for other potential applications, representing valuable steps in a proof-of-concept phase.

4.2.2. Illumination from mid-infrared interband cascade lasers

Under illumination from an ICL with wavelengths near 4.3 μm , the observed J-V characteristics for a device made from the same 7-stage IC wafer in Ref. [52] are shown in Fig. 7 for operation at 300 and 340 K [53]. The open-circuit voltage V_{oc} is 0.65 V at 300 K (with $J_{sc} = 1.4$ A/cm²), which is higher than a single bandgap determined value ($E_g/e \sim 0.25$ V) due to the 7 cascade stages. At 340 K, V_{oc} was still near 0.4 V (with a bandgap of 0.24 eV). Under the same illumination, J_{sc} is higher at 340 K because the reduction in bandgap causes a higher absorption coefficient at the same wavelength (4.3 μm). The bandgap-voltage offset W_{oc} decreases from 0.195 to 0.157 V with increasing illuminating power density (in Table 3), a trend expected from the theory [27]. However, the voltage efficiency η_v is less than 38% and FF is not high ($\leq 43\%$), as summarized in Table 3 for various input power densities and reflected by the shapes of the J-V curves. This may partially be caused by possible leakage current from the side walls due to imperfect device fabrication, as evidenced by the high saturation dark current density (410 mA/cm² at 300 K with an individual SL absorber thickness of only 0.15 μm) extracted from the experimental data [53]. Another factor is the thin metal contact layer (200–300 nm) along a relatively long path to the bonding pad, which adds a finite series resistance in the circuit and contributes to a low conversion efficiency ($\leq 2.1\%$). Also, in addition to a low absorbance of incident photons by a relatively thin total absorber layer, the photocurrent in every stage was not equal in these ICPV devices due to identical absorbers and consequently resulted in some absorbed photons not contributing to the photocurrent density. Hence, later ICPV devices were designed to achieve current matching [34,54-59] by choosing different individual absorber thicknesses d_m ($m = 1, 2, \dots, N_c$) based on $\eta_q = 1 - e^{-ad_1} = [1 - (m-1)\eta_q](1 - e^{-ad_m})$ with a given α determined by either an experiment or a theoretical calculation.

A two-stage and three-stage ICPV device structure, each with varied absorber thicknesses (~0.57–0.74 μm), were designed for approximate photocurrent matching between stages [55-57]. The first two absorbers

Table 2

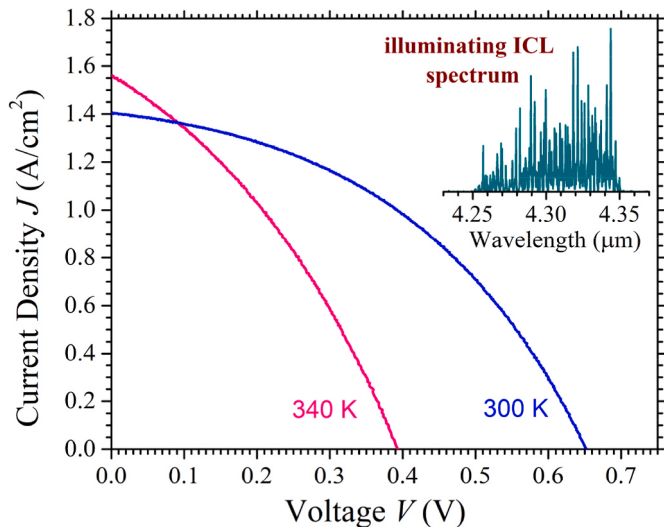
Performance characteristics of narrow bandgap ICPV cells under illumination from a BB source.

N_c	SL/QW ^a	E_g (eV)	T_c (K)	P_{in} (W/cm ²)	T_B (K)	J_{sc} (mA/cm ²)	V_{oc} (V)	W_{oc} (V)	η_v (%)	FF	η (%)	P_{out} (mW/cm ²)	Ref
7	SL	0.24	80	0.089	800	4.15	0.906	0.11	54	0.57	2.4	2.13	[51]
				0.218	1000	12.5	1.01	0.096	60	0.61	3.5	7.64	
				0.45	1200	29	1.08	0.086	64	0.62	4.3	19.4	
				0.67	1323	45	1.1	0.083	66	0.63	4.8	32	
11	QW	0.17			1323	4.9	0.52	0.123	26	0.42		1.1	[54]
				0.111	1323	6.35	1.63	0.077	75	0.463	4.3	4.8	
				0.0075	1200	0.341	1.47	0.10	67.7	0.446	3.0	0.23	
7	SL	0.31	80	0.0075	1200	<1.0	0.0057	0.259	0.22	<0.3		<0.002	[52]
^a Indicates absorber structures used in ICPV devices.													

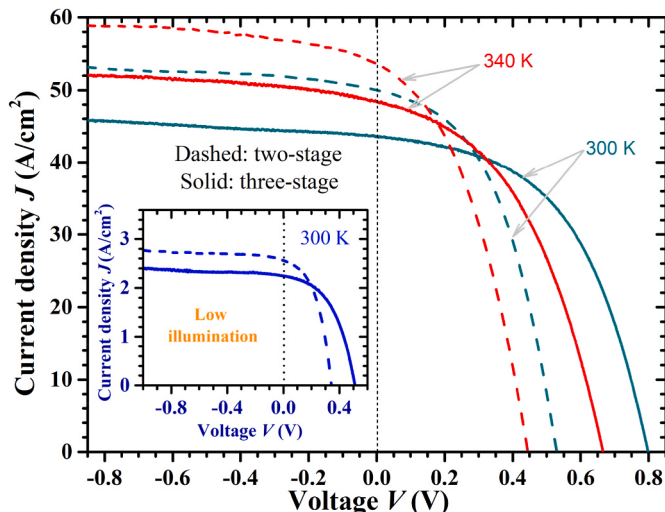
Table 3

Performance characteristics of narrow bandgap ICPV cells under illumination from ICLs.

N_c	SL/QW ^a	E_g (eV)	T_c (K)	P_{in} (W/cm ²)	J_{sc} (A/cm ²)	V_{oc} (V)	W_{oc} (V)	η_V (%)	FF	η (%)	P_{out} (mW/cm ²)	Ref
7	SL	0.25	300	5.02	0.38	0.386	0.195	22.1	0.35	1.01	52	[53]
				8.77	0.65	0.493	0.180	28.2	0.39	1.4	125	
				13.9	1.03	0.587	0.166	33.5	0.41	1.8	247	
				16	1.18	0.616	0.162	35.2	0.42	1.9	305	
				19	1.41	0.652	0.157	37.3	0.43	2.1	395	
2	SL	0.24	340	19	1.56	0.395	0.184	23.5	0.34	1.1	211	
				300	32.7	0.515	0.133	66	0.507	6.52	8544	[55–57]
3	SL	0.426	220	131	50	0.529	0.126	67.8	0.475	6.22	12563	
				300	62	0.726	0.148	58.3	0.706	205		
				141	32.9	0.784	0.129	62.1	0.530	9.03	5722	
2	SL	0.39	340	188	43.5	0.799	0.124	67	0.527	9.6	13580	
				48.4	0.666	0.158	0.178	68.3	0.514	9.5	17900	
				300	2.20	0.40	0.070	74.1	0.675	594		[54,55]
				2.95	0.107	0.177	0.177	23.3	0.328	104		
3	SL	0.27	150	2.23	0.594	0.072	0.129	73.3	0.685	907		
				300	2.99	0.153	0.179	22.2	0.328	150		
6	QW	0.38	293	2.77	0.0768	0.194	0.194	11.6	0.287	61		[65]
				10.7	6.27	0.058	0.167	25.8	0.264	0.90	96	
1	SL	0.225	300	36	12.6	0.085	0.14	37.8	0.252	0.75	270	[34]
				10.7	3.7	0.176	0.166	26.1	0.299	1.81	194	
5		0.225	340	36	12.2	0.271	0.135	40.1	0.275	2.5	905	
				10.7	3.05	0.207	0.173	19.3	0.328	1.93	207	
6	SL	0.214	300	36	9.3	0.371	0.14	34.7	0.377	3.6	1289	
				36	8.78	0.475	0.142	35.8	0.38	4.4	1584	
7		0.221	300	36	7.19	0.691	0.135	42.2	0.449	6.2	2232	[58,59]
7		0.234	36	36	0.691							

^a Indicates absorber structures used in ICPV devices.**Fig. 7.** J-V characteristics of an IC device at 300 and 340 K under illumination by an ICL with emission wavelengths near 4.3 μm (inset).

in both structures consisted of SLs with 100 and 113 InAs/GaSb/AlInSb/GaSb SL periods, which corresponds to absorber thicknesses of 570 nm and 644 nm, respectively. The third absorber SL in the three-stage wafer had 130 periods, corresponding to a thickness of 741 nm. The current density J versus voltage V is plotted in Fig. 8 for three-stage and two-stage devices at temperatures of 300 K and 340 K, under illumination from an ICL with a photon energy of ~0.44 eV. At 300 K, the maximum J_{sc} and V_{oc} for three-stage (two-stage) devices were 44 A/cm² (50 A/cm²) and 800 mV (530 mV), respectively. J_{sc} is lower in the three-stage device than in the two-stage device, indicating a photocurrent mismatch (e.g. ~15% at 300 K) between different stages. This can be improved by adjusting the individual absorber thicknesses. Nevertheless, a higher overall power conversion efficiency was achieved

**Fig. 8.** Measured J-V characteristics of representative ICPV devices at 300 and 340 K under a high-level of illumination from an ICL at a wavelength of 2.81 μm. Results for the devices at 300 K at a low-level illumination are inset.

by the three-stage device (9.6% vs 6.5% at 300 K), validating the benefits of having more stages in the multiple-stage architecture for narrow-bandgap TPV cells. Again, V_{oc} exceeded the single bandgap value ($E_g/e = 0.39$ V at 300 K) in both three- and two-stage devices, with the highest V_{oc} in the three-stage devices, demonstrating an effective cascade photovoltaic action in both multi-stage structures. Note that J_{sc} was increased by raising the device temperature (up to 340 K) in all devices under the same laser illumination level, which demonstrates the efficient collection of photo-generated carriers at high temperatures. Some performance characteristics for representative ICPV cells are summarized in Table 3.

Generally, as shown in Fig. 9, the output power density increases linearly and V_{oc} increases logarithmically with the input power density

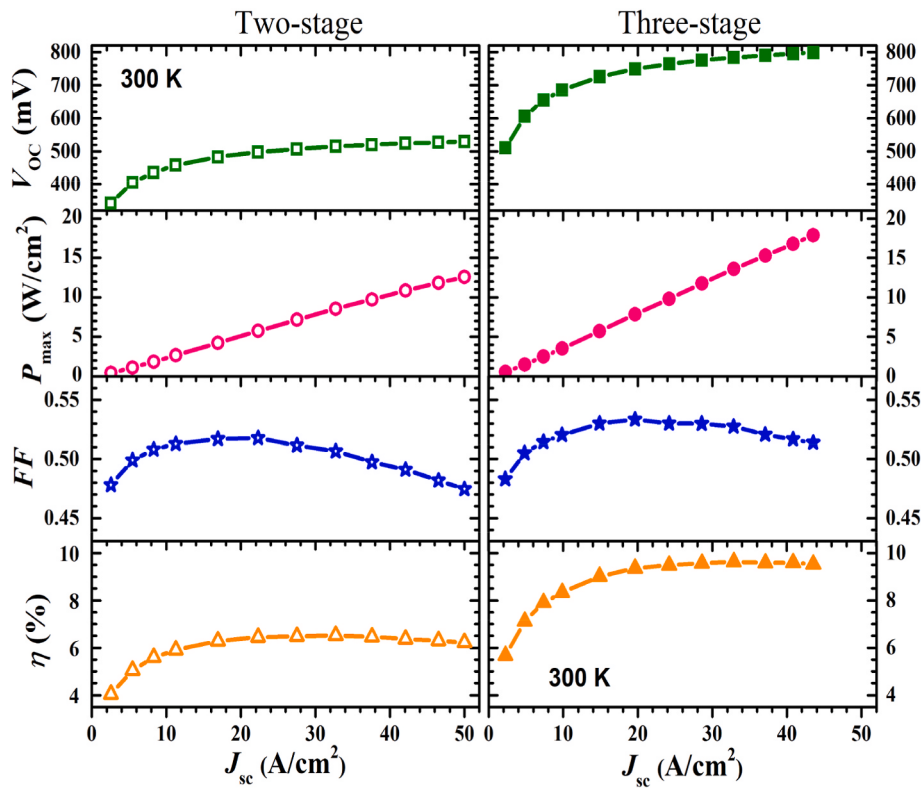


Fig. 9. V_{oc} (top), maximum output power density (upper mid), FF (lower mid), and conversion efficiency (bottom) as a function of J_{sc} for representative ICPV devices at 300 K.

of the light (embodied by a high J_{sc}). Note that η saturates at high illumination levels, then starts to exhibit a minor roll over along with a reduction of FF at higher J_{sc} in both three- and two-stage devices. However, this small efficiency drop at high J_{sc} was less in three-stage ICPV cells (1.1%) than in two-stage devices (4.6%). The lower J_{sc} , higher V_{oc} , and consequently lower ohmic losses in three-stage devices might be an important factor behind this behavior. The maximum in η occurs at $J_{sc} \sim 30 \text{ A}/\text{cm}^2$, which corresponds to an input power density that is not very high. The FF is still less than 53% for high J_{sc} , even though V_{oc} and η_v are reasonably high. This is again due to the high saturation dark current density J_0 for narrow bandgap materials at 300 K. When the device was operated at a lower temperature of 220 K, FF was about 71% even though J_{sc} was only $0.39 \text{ A}/\text{cm}^2$, as indicated in Table 3. Hence, it is important to reduce J_0 , which is related to material quality and device fabrication issues. The observed FF dependence on the device size [56] has suggested substantial leakage current from side walls due to imperfect passivation, which significantly affects device performance under a forward bias.

Another set of ICPV device structures with a narrower bandgap ($\sim 0.23 \text{ eV}$ at 300 K) was investigated for enabling energy conversion of longer-wavelength infrared photons. The set comprised 3- or 2-stage ICPV devices with varied InAs/GaSb SL absorber thicknesses to achieve a reasonable current matching between stages [54,55]. The two absorbers in the 2-stage ICPV structure were SLs of 126 periods ($\sim 605 \text{ nm}$) closer to the surface and 148 periods ($\sim 710 \text{ nm}$) closer to the substrate. The absorbers in the 3-stage structure had 132 ($\sim 634 \text{ nm}$), 157 ($\sim 754 \text{ nm}$) and 195 ($\sim 936 \text{ nm}$) periods, in order from the surface to the substrate. The total thickness of the absorber layers in the first two stages is only slightly larger ($\sim 5.5\%$) than that of the two-stage device. Under illumination of an ICL with an emission energy of $\sim 0.29 \text{ eV}$, nearly equal short-circuit current densities were obtained from the 3-stage and 2-stage devices as shown in Fig. 10. This suggests that both devices achieved a very high level of current matching ($>90\%$) between cascade stages at most of the measurement temperatures. For both

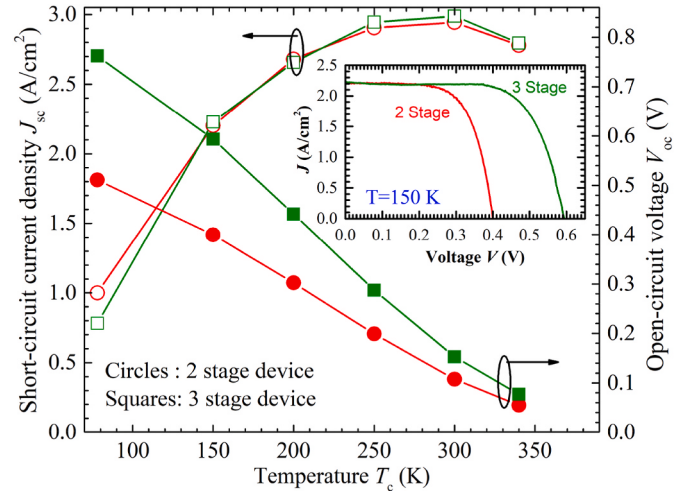


Fig. 10. J_{sc} and V_{oc} for representative ICPV devices at various operating temperatures. The inset shows their J-V characteristics at 150 K.

devices, J_{sc} increased as the temperature was raised from 78 to 300 K and decreased slightly as the temperature was subsequently raised to 340 K. The rise of the photocurrents with device temperature T_c was due to the increased absorption of photons as the bandgap decreased with increasing T_c . The decreasing photocurrent at 340 K may be due to the shorter diffusion length at higher temperature. The larger V_{oc} of a 3-stage device (153 mV at 300 K) compared to that of a 2-stage device (107 mV at 300 K) confirms that each additional stage contributes to a higher V_{oc} in a multi-stage ICPV device. At 78 K, the V_{oc} of 0.762 V for the 3-stage device was much higher than the single bandgap determined value ($\sim 0.289 \text{ V}$) with a η_v of $\sim 88\%$. The monotonic decrease in the V_{oc} values, as well as FF as given in Table 3, with increasing device

temperature T_c was mainly attributed to the higher dark current density and shorter carrier lifetime at higher temperatures. When the dark current density was negligible at low temperatures, the J-V characteristics were close to the ideal situation as shown in the inset to Fig. 10 for the two devices at 150 K. The FF of ~68% and other performance features are listed in Table 3. Also, it is worth pointing out that the observed voltage efficiencies η_v for the two sets of ICPV devices (having 2 or 3 stages) were nearly independent of N_c under the same level of illumination, consistent with the theory [38,39] mentioned in Section 4.2.1.

For the ICPV measurements discussed above, photons were incident on the top of the devices and the total absorber thickness was too thin ($\leq 2.3 \mu\text{m}$) to absorb all the incident photons. In the different configuration shown in Fig. 11, incident photons propagate along a waveguide perpendicular to the photocurrent in the vertical direction. As such, the incident photons that enter the absorbers are fully absorbed and current matching between stages is achieved. This was first demonstrated in a monolithically integrated mid-infrared ICL and photodetector configuration based on type-I InGaAsSb QWs ($E_g \sim 0.38 \text{ eV}$ at RT) and reported in 2016 [65]. An open-circuit voltage of 1.06 V was observed with $J_{sc} = 2.2 \text{ A/cm}^2$ and an output power density of 0.81 W/cm^2 (Table 3). This configuration has a potential application as an on-chip power convertor for future mid-infrared integrated circuits.

4.2.3. Collection efficiency and performance analysis

As discussed earlier, ICPV devices were expected in principle to circumvent the diffusion length limitation and therefore efficiently collect photo-generated carriers. To examine this, three ICPV structures shown in Fig. 12 were designed with InAs/GaSb SL absorbers and grown by MBE [34]. The absorber thickness for the 1-stage device is $2.31 \mu\text{m}$. The 3-stage device has a total absorber thickness (d_{total}) equal to that of the 1-stage device with discrete individual thicknesses of 624, 749 and 936 nm from the surface to the substrate. The individual absorber thicknesses in the 5-stage device are somewhat thinner (see Fig. 12) and the d_{total} is $2.52 \mu\text{m}$, slightly thicker than the 1- and 3-stage devices. With different individual absorber thicknesses, the collection efficiency η_c of photo-generated carriers could be extracted from measurement of photocurrent.

Based on the cutoff wavelengths of photo-response spectra, the bandgaps of the three PV devices at 300 K were determined to be 225 meV for the 3- and 1-stage devices, and 214 meV for the 5-stage device [34]. An ICL with an emission wavelength near $4.25 \mu\text{m}$ was employed to illuminate the three PV devices from the top. The ICL's emission wavelength corresponds to a photon energy of 291 meV, which is 60–80 meV higher than the bandgaps of the ICPV devices at 300 K. At this

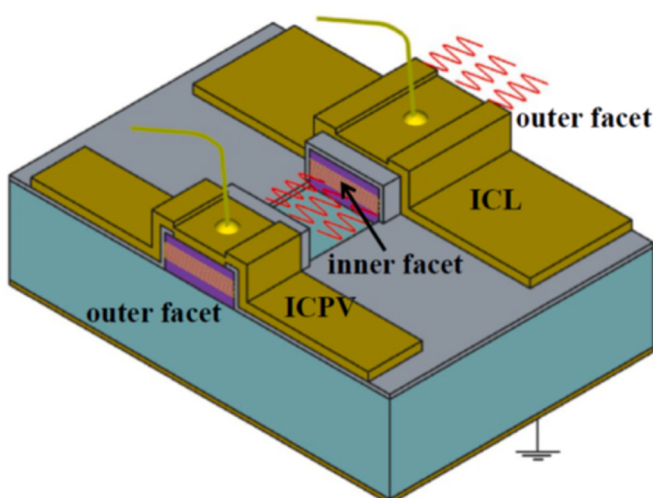


Fig. 11. Illustration of an ICL and ICPV device on the same chip.

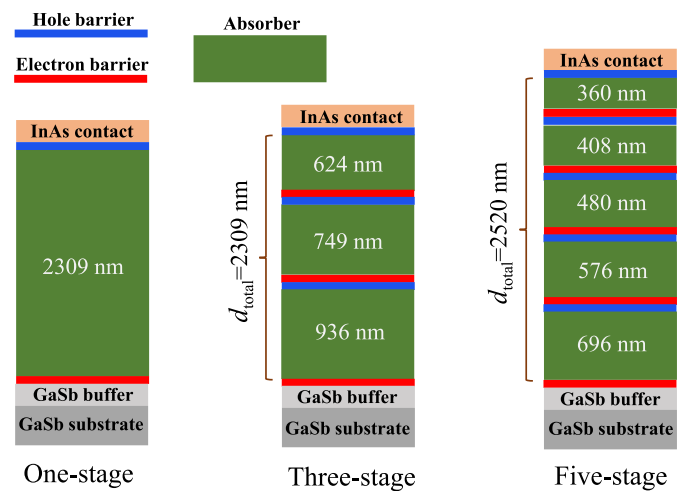


Fig. 12. Schematic layer structures of the three ICPV devices with one, three and five stages.

wavelength, the photocurrent was effectively matched in the 5- and 3-stage devices. The performance of the three PV devices was investigated for different levels of illumination by adjusting the injection current of the ICL. Fig. 13(a) shows the J-V curves of the three devices when illuminated at a medium P_{in} of 19 W/cm^2 [34]. The solid curves are the

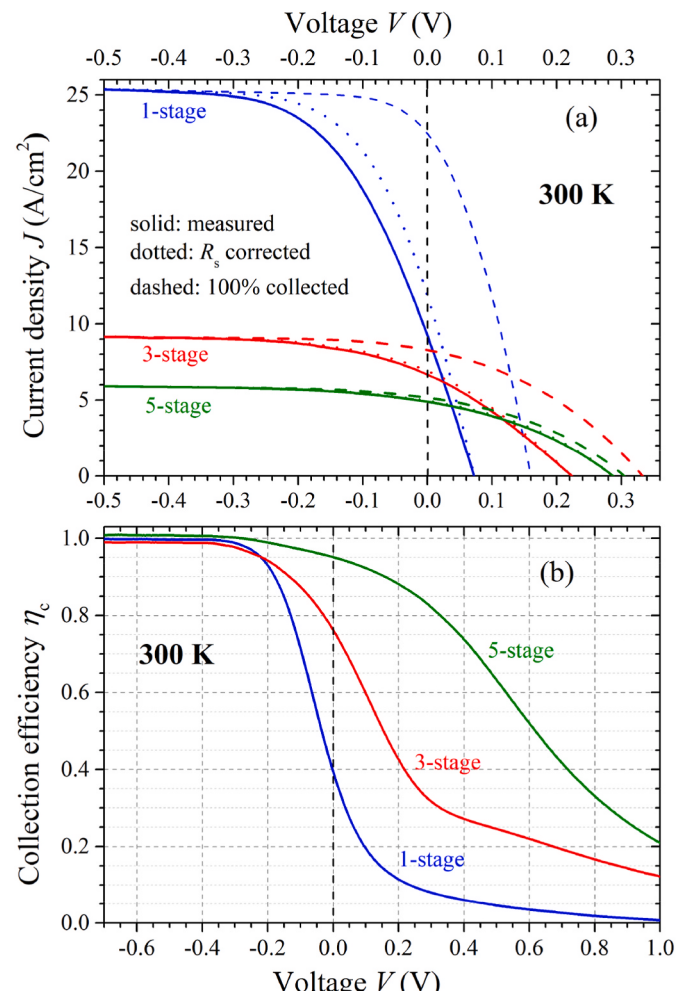


Fig. 13. (a) J-V characteristics and (b) collection efficiency of the 1-, 3- and 5-stage devices at 300 K under an illumination level of 19 W/cm^2 .

measured J - V curves, the dotted curves are corrected to remove the loss due to the series resistance (R_s), and the dashed curves correspond to the case where the photo-generated carriers are assumed to be 100% collected. The series resistances of the three devices were extracted by linear fitting of dV/dI - I curves where the fitted parameter for the intercept equals the series resistance [66]. The 100% collected J - V curves are the superposition of the dark current density (J_d) and J_{phmax} . The magnitude of J_{phmax} is the difference between the saturated current densities under dark and illuminated conditions. As shown in Fig. 13(a), the photocurrent density (J_{ph}) is highest for the 1-stage device, followed by the 3-stage device and finally the 5-stage device, as expected since J_{ph} is proportional to the individual absorber thickness. The short-circuit current density in the 1-stage device is noticeably increased when a correction is applied for R_s . The R_s -corrected J - V curves for the 5- and 3-stage devices almost coincide with the measured J - V curves because of the lower current densities compared to the 1-stage device.

An inspection of the measured and 100% collected J - V curves in Fig. 13(a) shows that the photocurrent in the devices is voltage dependent. In other words, the shift between the measured and 100% collected J - V curves arises from the voltage-dependent photocurrent (or collection efficiency) in the three devices. The 1-stage device has the largest shift between measured and 100% collected J - V curves. The shift is also significant for the 3-stage device, while it is small for the 5-stage one. This implies that the illuminated J - V curves are not obeying the standard superposition principle [67], and the collection efficiencies and the photocurrents are voltage dependent in the three devices. Therefore, the photocurrent should not be preserved as a voltage independent constant as in the commonly used standard model [67]. The voltage-dependent collection efficiency η_c (V) can be obtained through an approach described in Refs. [68,69] with different illumination levels and is shown in Fig. 13(b) for the three devices [34]. The 5-stage device has the highest η_c (V) because the individual absorbers are thin, so the photo-generated carriers only need to travel a short distance before they are collected. The η_c (V) is lowest in the 1-stage device because it has the thickest single absorber among the three devices, which contributes to

the lowest FF (Fig. 14) in addition to a larger series resistance loss. The highest η_c (V) of the 5-stage device leads to the highest η among the three devices. The value of η at the maximum P_{in} of 36 W/cm^2 is 3.6%, 2.5% and 0.8% for the 5-, 3- and 1-stage devices at 300 K, respectively. Their device performance features are shown in Fig. 14 [34] and Table 3. The fill factor for the 1- and 3-stage devices decreased when $P_{in} \geq 10 \text{ W/cm}^2$, which is somewhat similar to what was shown in Fig. 9 where the illumination level was much higher ($P_{in} > 100 \text{ W/cm}^2$). The conversion efficiency for the 1-stage device approached a saturation at a relatively low P_{in} and exhibited a drop (16%) after saturation, while η had not yet saturated for the 5- and 3-stage devices. These results unambiguously demonstrate the advantage of multi-stage ICPV devices over conventional single-stage PV devices. It was noticed that the voltage efficiency η_v in the 5-stage device was unexpectedly lower, especially at low illumination levels as cited in Table 3. This might be due to the narrower bandgap and some variations in material quality, which substantially increased the thermal generation rate (about two times higher at 300 K based on the measured characteristics of dark current density and calculations) compared to the 3-stage device [34].

As ICPV devices were projected theoretically to perform better with more cascade stages and thin individual absorbers, and verified experimentally with significantly improved collection efficiency and overall performance, four ICPV structures were designed and grown by MBE based on nominally identical InAs/GaSb SL absorber units, but with different thicknesses and numbers of cascade stages [58,59]. As shown in Fig. 15, the first two structures have 6 and 7 stages and were grown earlier. The other two structures have substantially more stages (16 and 23) with thinner absorbers and were grown a year later after a maintenance cycle for the MBE system. The 6- and 7-stage ICPV wafers were first fabricated into devices. Although there were some variations in material growths, resulting in somewhat different bandgaps (221 meV and 234 meV for the 6- and 7-stage devices at 300 K, respectively), under illumination from the same ICL near 4.2 μm , the device performances are better than for the previous 5-stage ICPV device. For example, at $P_{in} = 36 \text{ W/cm}^2$, the V_{oc} is 371, 475 and 691 meV for the 5-stage, 6-stage

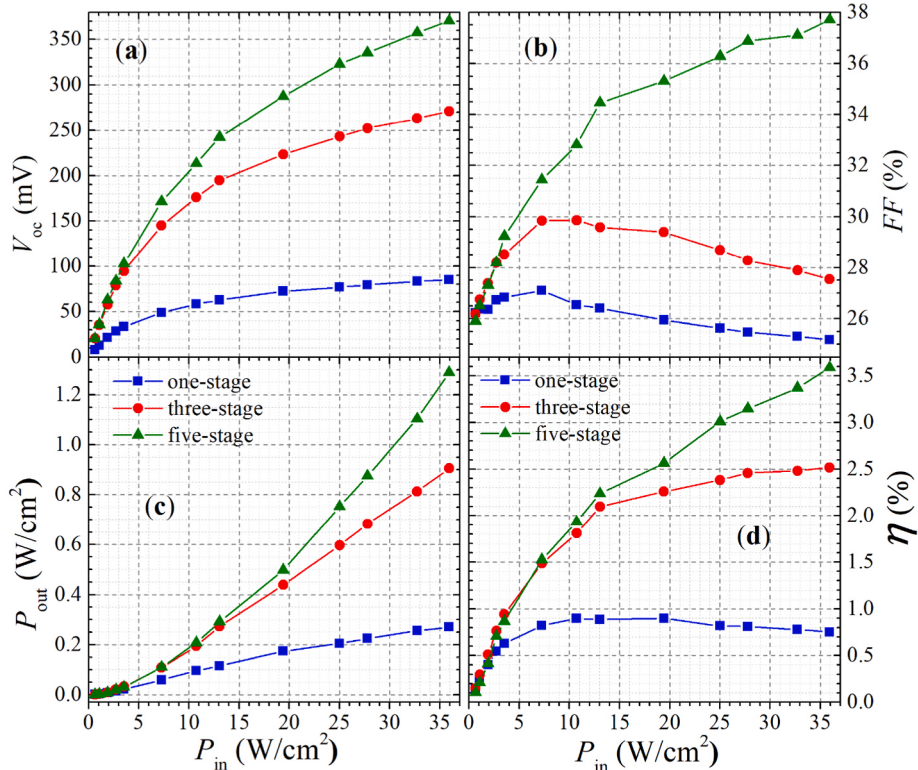


Fig. 14. (a) V_{oc} , (b) FF , (c) P_{out} and (d) η as a function of P_{in} for the three devices at 300 K.

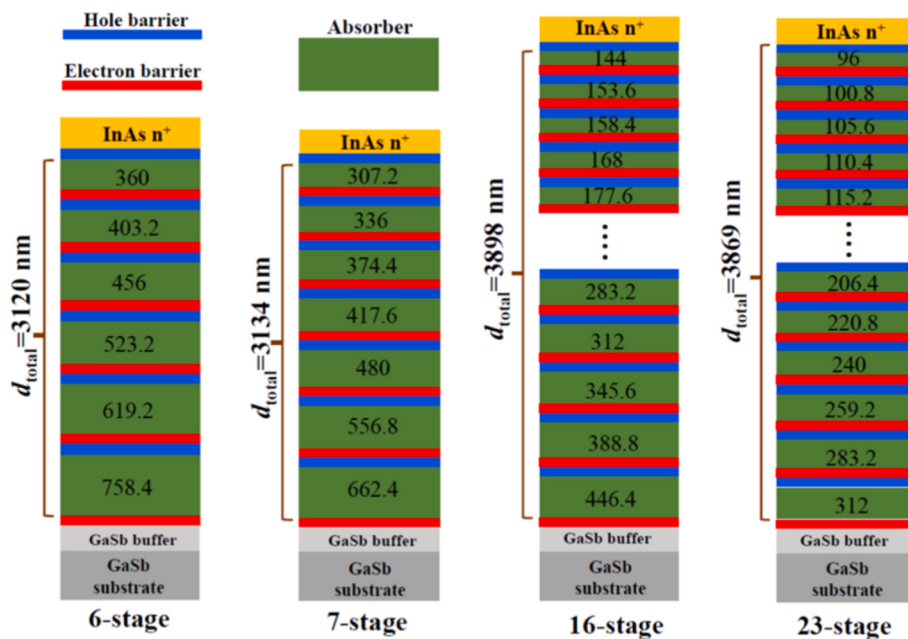


Fig. 15. Schematic layer structures of the four ICPV devices with 6, 7, 16 and 23 stages.

and 7-stage devices at 300 K, respectively, with corresponding voltage efficiency of 34.7% (5-stage), 35.8% (6-stage) and 42.2% (7-stage) and corresponding FF of 37.7%, 38.0% and 44.9% [58]. These factors resulted in higher conversion efficiencies of 4.4% and 6.2%, and output power densities of 1.6 W/cm² and 2.2 W/cm² for the 6- and 7-stage devices, respectively, as indicated in Table 3.

PV devices were fabricated later from the 16- and 23-stage wafers. Under illumination from the same ICL near 4.2 μm, even though the bandgaps are somewhat larger due to variations of material growths (248 and 243 meV for the 23- and 16-stage devices at 300 K, respectively), their conversion efficiencies were unexpectedly lower than those obtained for the 7- and 6-stage devices [59]. For example, at $P_{\text{in}} = 21$ W/cm², the η was 3.3% and 2.7% for the 27- and 16-stage devices at 300 K, respectively, compared to 4.1% and 3.5% obtained from the 7- and 6-stage devices at 300 K. These results contradict the theoretical projection [38,39] and previous experimental findings mentioned above. Nevertheless, η was higher for devices with more stages if the devices were grown in the same campaign, *i.e.* the device performance is better for the 23-stage than the 16-stage, and for the 7-stage than the 6-stage.

In Ref. 59, a detailed characterization and performance analysis was presented for these four narrow bandgap (~0.22–0.25 eV at 300 K) ICPV devices. The carrier lifetime was extracted to analyze how the material quality (including device fabrication quality) affects the device performance. By extracting the carrier lifetime from the measured dark current density and comparing all the factors with quantitative analysis, it was shown that the material quality, which often limits the carrier lifetime, has the most substantial impact on the device performance among all the factors. It should be noted that the device fabrication quality also significantly affects device performance and the extracted value of the carrier lifetime through an electrical method [70]. Substantial leakage current through side walls due to possible imperfect passivation would increase the saturation dark current density, reduce FF and lower the voltage efficiency, resulting in a low conversion efficiency and a shortened carrier lifetime. Hence, the material quality mentioned in Ref. 59 should include the device fabrication quality. Also, it was shown that current mismatch between stages could be considerable with more stages due to the variation of absorption coefficient. On the other hand, the collection efficiency η_c of photo-generated carriers can be improved substantially with thin individual absorbers and more stages. The extracted shorter carrier lifetime (28 ns for 16- and 23-stage devices

versus 86 and 88 ns for 6- and 7-stage devices respectively), combined with substantial current mismatch, elucidated the lower conversion efficiencies in the 16- and 23-stage devices compared to that in the 6- and 7-stage ones. The analysis further revealed that although the current mismatch is more significant in the 23- and 16-stage devices, the conversion efficiency η would be higher in the 23- and 16-stage devices than in the 7- and 6-stage ones if the carrier lifetime could be kept the same [59].

4.3. Resonant cavity enhanced ICPV cells

As already discussed above, narrow bandgap ICPV cells can circumvent the diffusion length limitation to have a high collection efficiency η_c and consequently an increased conversion efficiency η . However, both modeling and experimental results have also shown that the high dark saturation current density J_0 remains a major issue. Besides intrinsically high carrier concentrations in narrow bandgap semiconductors, the high J_0 is due mainly to the short carrier lifetime in the InAs/GaSb SL absorbers, which caused a small FF and a low η_v and consequently limited the conversion efficiency η . To alleviate this issue, the ratio of the photocurrent density to the J_0 needs to be increased without an increase in the incident photon intensity. This can be achieved by placing an ICPV cell in a resonant cavity where multiple reflections can build up a high intensity optical field. The high intensity will enhance the ICPV cell's optical absorption and quantum efficiency, resulting in an increased photocurrent density while keeping J_0 at the same level. This approach was recently proposed and investigated [71, 72]. Simulations with realistic material parameters based on InAs/GaSb SL heterostructures, showed that resonant cavity enhanced (RCE) ICPV cells were theoretically capable of achieving a η beyond 60% [72], which is far higher than any other approach can achieve, especially when the absorber bandgap is smaller than 0.3 eV. This approach bears some similarities in philosophy and spirit with the light trapping concept in PV cells [73,74]. However, one important difference is that RCE ICPV cells must be optimized for a single wavelength and therefore will not be applicable to broadband radiation sources. Before discussing the simulation results in detail for RCE ICPV cells, a brief background will be given.

RCE PV cells are closely related to RCE photodetectors, which have been studied widely in the near-IR spectrum [75,76] and were recently

demonstrated in the mid-IR regime [77] with a high QE. A RCE detector typically has a single absorber that is positioned at an antinode of a cavity. In a few special cases, the detector contained multiple absorbing layers located at different antinodes of a cavity. For instance, a detector reported in Ref. [78] was composed of three absorbers (in separate antinodes of a cavity) and its QE was 30% higher than that of a single-absorber detector with a comparable overall thickness. The three absorbers in the detector were connected in series within a single junction, not as separate stages connected by interband tunnel junctions. The device operated essentially like a conventional single-junction PV device, where a higher dark current density is produced by adding up the thermally generated carriers created in each absorber. This is not a favorable way for a PV cell where the dark current density should be minimized. This issue can be circumvented by partitioning the absorber into discrete interband cascade stages, each located at a different antinode of a cavity. In this architecture, a higher V_{oc} is produced by adding up the voltages created in each stage while the dark current density is determined only by a single absorber. The dark current density can be kept relatively low by using thin individual absorbers. In this way, the ICPV device trades current for a higher output voltage. Since the photocurrent is normally significantly higher than in a solar cell, the trade-off is especially beneficial in reducing the power lost through the series resistance.

4.3.1. Quantum efficiency and particle conversion efficiency

In ideal RCE ICPV cell, a standing wave is formed in a cavity and the light intensity at each antinode is equal. Hence, the individual absorbers in each stage should made identical, and they should be located precisely at the antinodes. Therefore, the effective QE at the resonant wavelength is the same for each stage, and given by the following equation [72,76]:

$$\eta_q = \frac{1 + R_2 e^{-\alpha_{eff} N_c d}}{(1 - \sqrt{R_1 R_2} e^{-\alpha_{eff} N_c d})^2} (1 - R_1) (1 - e^{-\alpha_{eff} d}) = QEF (1 - e^{-\alpha_{eff} d}) \quad (3a)$$

$$QEF = \frac{1 + R_2 e^{-\alpha_{eff} N_c d}}{(1 - \sqrt{R_1 R_2} e^{-\alpha_{eff} N_c d})^2} (1 - R_1) \quad (3b)$$

where R_1 (R_2) is the mirror reflectance at the top (bottom) of the optical cavity and d is the thickness of an individual absorber. Note that Eq. (3a) is not exactly the same as the equation given in Ref. [76] because of the important difference between the cascade and conventional detector configurations that was discussed earlier. The QE enhancement factor (QEF) is introduced to quantify the augmentation of the η_q by multiple reflections of the light wave in the cavity. Additionally, the standing wave effect (SWE) is included in Eq. (3) through the effective absorption coefficient $\alpha_{eff} = SWE \cdot \alpha$, where the SWE boosts the one-pass light absorption coefficient. The SWE is a measure of the overlap between the light field in the cavity and the individual absorber. The SWE is substantial when the absorbers are thin in an RCE ICPV cell. On the other hand, the SWE can be neglected when the absorbers are thick. At the resonant condition, the SWE is given by Ref. [76]:

$$SWE = 1 + \frac{2r_2 \sin(\beta d)}{\beta d (1 + R_2)} \quad (4)$$

where β is the propagation constant ($=2\pi n/\lambda_0$, where λ_0 is the incident wavelength and n is the refractive index) and r_2 is the magnitude of the bottom mirror reflectivity. According to Eq. (4), the SWE reaches its maximum value (~ 2) when the absorber approaches zero thickness ($d \rightarrow 0$) and is located precisely at an antinode of a cavity. The SWE decreases with increasing d with a lower limit of 1.

As the absorber is made thicker, as discussed earlier the collection efficiency of photo-generated carriers may be reduced depending on the diffusion length L . Note that Eq. (3a) is valid only when L is substantially longer than the absorber thickness. For real narrow bandgap materials,

the formula may overestimate η_q . Hence, Eq. (3a) should be modified to include the effect of a finite diffusion length and can be rewritten as:

$$\eta_q = QEF \frac{\alpha_{eff} L}{1 - (\alpha_{eff} L)^2} \left[\tanh(d/L) - \frac{\alpha_{eff} L \exp(-\alpha_{eff} d)}{\cosh(d/L)} - \alpha L \right] \quad (5)$$

The calculated η_q versus d for two values of N_c is shown in Fig. 16 based on Eq. (3a) and Eq. (5), where the reflectance of the bottom mirror is $R_2 = 0.9$, while the top mirror reflectance R_1 is 0.7 or 0.3. Here, $\alpha = 3000 \text{ cm}^{-1}$ and $\lambda_0 = 4 \mu\text{m}$ [72]. As shown in Fig. 16, the calculated η_q based on Eq. (3a) and Eq. (5) nearly overlap with each other, since the d ($< 500 \text{ nm}$) is considerably shorter than the diffusion length ($1.5 \mu\text{m}$ for SL absorbers with $E_g = 0.28 \text{ eV}$). This indicates that the inclusion of a finite L in Eq. (5) makes little difference on the value of η_q for RCE ICPV cells, which echoes the advantage of a high collection efficiency for the ICPV architecture.

From Fig. 16, it is clear that the improvement of η_q by the optical cavity is very significant at the resonant wavelength. For example, a 2-stage RCE ICPV cell with $R_1 = 0.7$ has a maximum η_q of 65% when the absorber thickness is 228 nm. When R_1 for the 2-stage RCE ICPV cell is reduced to 0.3, the η_q peaks at a lower value (52%) and for a thicker individual absorber (332 nm). Even with the thinner individual absorbers for the 6-stage ICPV cells, the peak η_q exceeds 27%. All these η_q values are far higher than for regular ICPV cells, where the maximum η_q is only about 13% under the same conditions [39]. The significant improvement of η_q by the optical cavity results in a remarkable increase in power conversion efficiency η as shown later in sub-Section 4.3.2. For each value of N_c , the η_q declines after the peak value with a further increase of d , as expected from the light intensity attenuation with increased absorption. This attenuation is described by the first fractional term in Eq. (3b), which decreases with increasing d . For the same reason, the η_q decreases with N_c (Fig. 17) as the light absorption increases with more stages and consequently the light intensity is reduced in the cavity. Nevertheless, the particle conversion efficiency η_{part} increases with N_c as shown in Fig. 17 [72], and can exceed 100% due to multiple reflections of a wave (and the SWE) and is a more appropriate measure for power conversion efficiency as indicated by Eq. (2). From Fig. 16, there is an optimal individual absorber thickness that maximizes the η_q of an RCE ICPV cell for a given N_c . Consequently, there is also an optimal individual absorber thickness $d_{optimal}$ that maximizes the η of an RCE ICPV cell for a given N_c [72].

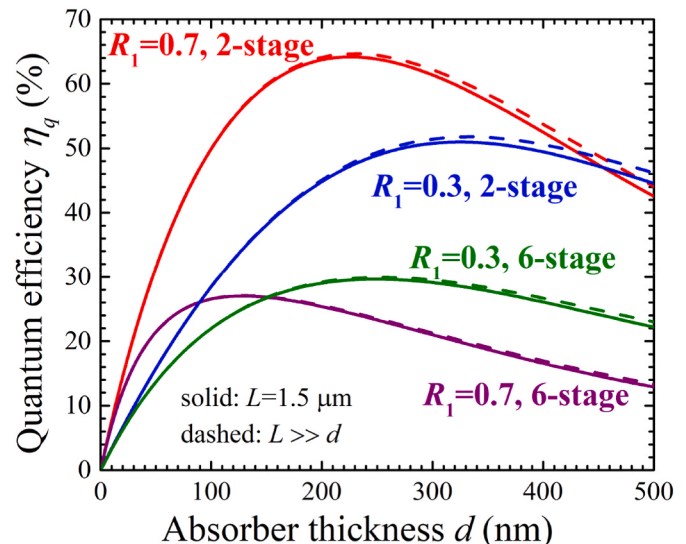


Fig. 16. Calculated η_q based on Eq. (5) (solid) and Eq. (3) (dashed) as a function of d with different N_c and R_1 .

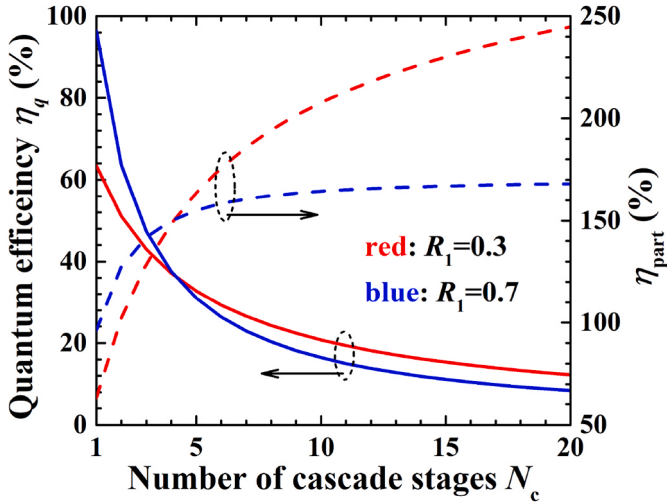


Fig. 17. QE and η_{part} (particle conversion efficiency) of optimized RCE ICPV cells at 300 K.

4.3.2. Conversion efficiency

Based on InAs/GaSb T2SL absorbers with $E_g = 0.28$ eV, the calculated power conversion efficiency η for RCE ICPV cells is shown in Fig. 18 along with FF and voltage efficiency. FF and η_v decrease with N_c because the light intensity drops with more absorption, but do so quite slowly and nearly saturate at a large N_c as shown in Fig. 18(a). From

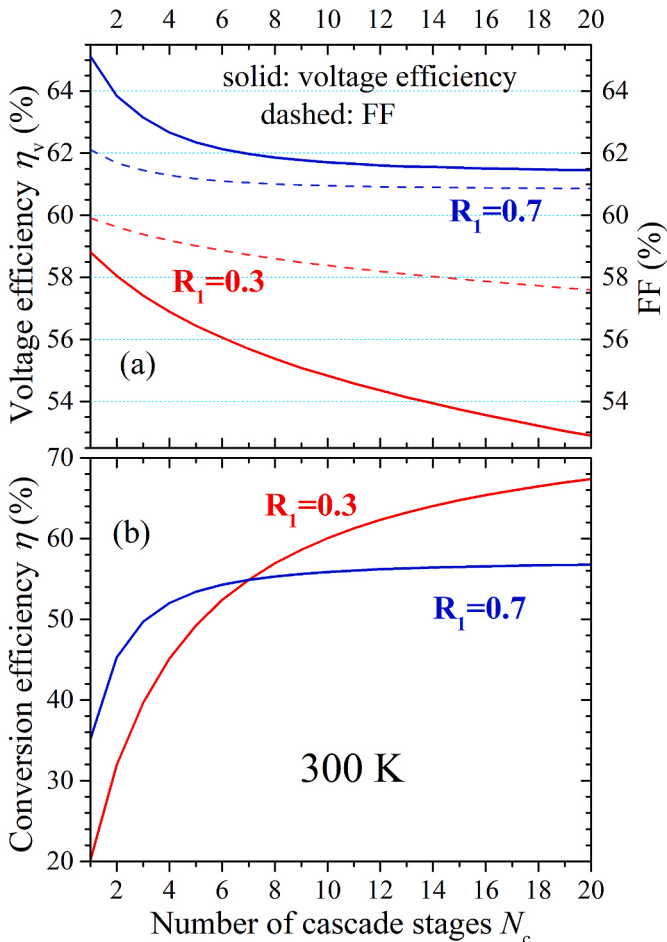


Fig. 18. (a) FF and voltage efficiency η_v of optimized RCE ICPV cells and (b) Maximum conversion efficiency vs. N_c . $P_{in} = 50$ W/cm².

Fig. 18 (b), η and η_{part} (Fig. 17) follow nearly the same trend with increasing N_c , which further verifies the validity of Eq. (2). The maximum η gained by RCE ICPV cells with large N_c are 57% and 67% for $R_1 = 0.7$ and $R_1 = 0.3$, respectively. These values of η are several times larger than that of a regular ICPV cell, which has a maximum η of only 15% under the same conditions [72], even though the FF and voltage efficiency η_v are still not high as shown in Fig. 18(a). This could be further understood by expressing η as:

$$\begin{aligned}\eta &= FF \times \eta_q \times qV_{oc}/hv = FF \times (N_c \times \eta_q) \times eV_{oc}/(N_c \times hv) \\ &= FF \times \eta_{part} \times \eta_v \times \eta_p,\end{aligned}\quad (6)$$

where hv is the photon energy and $\eta_p = E_g/(hv)$ is the photon energy efficiency, which is nearly 100% when the photon energy is close to the bandgap. Because η_{part} can exceed 200% in a resonant cavity as shown in Fig. 18, η in Eq. (6) can be more than 60%, although FF and η_v remain below 65%. The high power-conversion efficiency unambiguously demonstrates the great potential and benefits of RCE ICPV cells. However, the implementation of RCE ICPV cells is challenging because precise control of layer thicknesses and locations is required. The demonstration of RCE ICPV cells has not yet been reported. Nevertheless, RCE mid-IR photodetectors [77] and interband cascade vertical cavity surface emitting lasers [79,80] with similar requirements have been demonstrated using the InAs/GaSb/AlSb material system. So, it should be feasible to realize RCE ICPV cells with the current technology for MBE growth and device fabrication.

5. Outlook and concluding remarks

The utilization of low energy radiative photons from various sources could have immense impact on energy and environmental issues. Nevertheless, a review of the literature on narrow bandgap (<0.5 eV) materials for TPV applications makes it clear that the relevant research activities have been very limited. This is related to both fundamental and technological challenges in narrow bandgap materials – *i.e.* intrinsically high carrier concentration, low absorption coefficient, relatively poor material quality and less mature device fabrication compared to wide bandgap materials such as GaAs- and InP-based III-V semiconductors. Therefore, TPV cells made so far from bulk narrow bandgap III-V materials have a low voltage efficiency (<40%) and a low fill factor (<0.4), resulting in a low power conversion efficiency (<4%) for room temperature operation.

Other types of narrow bandgap materials, such as MCT and lead salts, have been used for photodetectors, but their use for TPV applications has not been reported. Since the bonding of atoms in II-VI and IV-VI compounds is weaker than in III-V semiconductors, material uniformity and thermal expansion may be serious concerns for large area TPV cells. Alternatively, TPV devices based on intraband quantum cascade (QC) structures [81,82] have been proposed. Their experimental demonstration has not been reported yet, perhaps because the carrier lifetime in intraband QC structures is very short (~ps). This would result in a very small open-circuit voltage and a high saturation current density [83].

The multi-stage interband cascade architecture that emerged from mid-IR semiconductor laser research can circumvent or alleviate some of the inherent problems in narrow bandgap PV cells. These include the low absorption coefficient and short diffusion length limitation. As such, a high collection efficiency for photo-generated carriers with a nearly 100% particle conversion efficiency can be achieved in a regular PV configuration. Additionally, by trading current for a high operating voltage, the series resistance loss can be mitigated. Because the short transport distance enables a high collection efficiency, ICPV cells can handle high levels of light illumination without a saturation of the output power density. These advantages of multi-stage ICPV cells have been verified by theoretical modeling and demonstrated experimentally by preliminary ICPV devices that were not optimized. The absorbers in

these ICPV devices were engineered InAs/GaSb T2SLs, in which the bandgap can be tailored across the entire mid-IR spectrum by adjusting the layer thicknesses within the SL period rather than by changing the bandgaps of the constituent materials.

InAs/GaSb T2SLs have been recently employed extensively for mid- and long-wave IR photodetectors and focal plane arrays [84,85]. The material growth and device fabrication technologies involved with detectors and lasers based on this T2SL materials likely can be leveraged for the research and development of ICPV cells. However, the carrier lifetime in InAs/GaSb T2SLs is short (several to tens of ns [70,86]) and their saturation dark current density J_0 is high, which causes a small fill factor and a low voltage efficiency as shown earlier, resulting in a low power conversion efficiency. This might be a major reason why a high open-circuit voltage (>50 mV) has not been observed from a narrow bandgap ICPV device at room temperature under illumination from a broadband heat source such as a blackbody radiation source. This issue could be partially alleviated in a near-field TPV configuration where QE and photocurrent density can be enhanced significantly without increasing the dark current density, likely resulting in higher open-circuit voltage and conversion efficiency.

To overcome the short carrier lifetime in InAs/GaSb T2SLs, the absorbers could instead be Ga-free InAs/InAsSb SLs, which have been demonstrated to have a relatively long carrier lifetime (several μ s) [86–88]. Hence, combining InAs/InAsSb SL absorbers with the interband cascade structure would enable a significant increase in the conversion efficiency (possibly by more than 15%). To date, however, an InAs/InAsSb SL has not been incorporated into an interband cascade structure. How it can be smoothly integrated with the interband cascade structure and related carrier transport need to be investigated and understood. Additionally, since InAs/InAsSb SLs have been studied for photodetector applications mainly at low temperatures, their properties at high temperatures (e.g. room temperature) are not well known. Therefore, extensive studies of InAs/InAsSb SLs at room temperature and characterization of how their properties depend on temperature are required before they can be optimized for practical devices. Even though the absorption coefficient of the InAs/InAsSb SL is relatively small, the effects can be alleviated with the interband cascade structure.

Another aspect that remains to be explored is the integration of discrete individual absorbers with different bandgaps into an interband cascade structure to harness radiative photons from a broadband heat source. Not only will the power conversion efficiency be increased, but also the output power density will be enhanced. In addition to the T2SLs, type-I SLs and GaInAsSb bulk materials [89] can be used as absorbers. ICLs have been successfully demonstrated with both type-II and type-I QWs covering the wavelength region from 2 to 11 μ m [90,91]. Hence, it is feasible to integrate different discrete absorbers into an interband cascade structure. Certainly, this is a complicated task considering the current matching requirement between many stages.

In reviewing progress on narrow bandgap photovoltaic cells, it is evident that researchers in this field face multiple challenges. Several important limitations of a single p-n junction device have been alleviated by employing the interband cascade architecture, where multiple absorbers are connected in series by interband tunnel junctions by taking the advantage of natural type-II broken gap alignment in InAs/GaSb/AlSb material system. However, a needed improvement in the ratio of photocurrent to dark current has not yet been sufficiently realized. Absorber integration within a resonant cavity and potentially new materials for the superlattice absorber offer opportunities to extensively address this challenge with interband cascade PV devices. Additionally, appropriate light trapping structures [73,74] can be developed in combination with the ICPV configuration for broadband radiative sources in TPV system. While significant challenges remain in developing practical TPV systems with narrow bandgap materials, promising solutions for each of these challenges are currently being considered and pursued.

Declaration of competing interest

The authors declare that they have no known competing financial interests or personal relationships that could have appeared to influence the work reported in this paper.

Acknowledgements

The authors are grateful for the support they have received from the DOE EPSCoR program (Award No. DE-SC0004523) and the National Science Foundation (NSF) under Grant DMR-1608224. They thank their collaborators John F. Klem, Robert T. Hinkey, Lu Li, Hossein Lotfi, Hao Ye, Lin Lei, Zhaobing Tian, Yuzhe Lin, Jeremy A. Massengale, S.M. S. Rassel, Joel C. Keay, Tetsuya D. Mishima, and Matthew B. Johnson for their contributions to some of the work that was described in this article, and Qi Lu for providing some data for InAs TPV cells in Table 1. Also, they would like to thank one of the reviewers for bringing to their attention the concept of bandgap-voltage offset in Ref. [27].

References

- [1] M.G. Mauk, "Survey of thermophotovoltaic (TPV) devices," chap. 21, in: A. Krier (Ed.), *Mid-infrared Semiconductor Optoelectronics*, Springer, Berlin, 2006.
- [2] D.L. Chubb, *Fundamentals of Thermophotovoltaic Energy Conversion*, Elsevier Science, Amsterdam, 2007.
- [3] T. Bauer, *Thermophotovoltaics: Basic Principles and Critical Aspects of System Design*, Springer, Berlin, 2011.
- [4] A. Datas, C. Algora, Global optimization of solar thermophotovoltaic systems, *Prog. Photovoltaics Res. Appl.* 21 (No. 5) (2013) 1040.
- [5] T.J. Coutts, A review of progress in thermophotovoltaic generation of electricity, *Renew. Sustain. Energy Rev.* 3 (1999) 77.
- [6] N.-P. Harder, P. Würfel, Theoretical limits of thermophotovoltaic solar energy conversion, *Semicond. Sci. Technol.* 18 (2003) S151.
- [7] E. Rephaeli, S. Fan, Absorber and emitter for solar thermophotovoltaic systems to achieve efficiency exceeding the Shockley-Queisser limit, *Opt Express* 17 (2009) 15145.
- [8] S. Molesky, C.J. Dewalt, Z. Jacob, High temperature epsilon-near-zero and epsilon-near-pole metamaterial emitters for thermophotovoltaics, *Opt Express* 21 (2013) A96.
- [9] W. Shockley, H. Queisser, Detailed balance limit of efficiency of p-n junction solar cells, *J. Appl. Phys.* 32 (1961) 510.
- [10] C.A. Wang, H.K. Choi, S.L. Ransom, G.W. Charache, L.R. Danielson, D.M. Depoy, High-quantum-efficiency 0.5 eV GaInAsSb/GaSb thermophotovoltaic devices, *Appl. Phys. Lett.* 75 (1999) 1305.
- [11] C.A. Wang, R.K. Huang, D.A. Shiao, M.K. Connors, P.G. Murphy, P.W. O'Brien, A.C. Anderson, D.M. Depoy, G. Nichols, M.N. Palmisiano, Monolithically series-interconnected GaInAsSb/AlGaAsSb/GaSb thermophotovoltaic devices with an internal backsurface reflector formed by wafer bonding, *Appl. Phys. Lett.* 83 (2003) 1286.
- [12] R.K. Huang, R.J. Ram, M.J. Manfra, M.K. Connors, L.J. Missaggia, G.W. Turner, Heterojunction thermophotovoltaic devices with high voltage factor, *J. Appl. Phys.* 101 (2007), 046102.
- [13] R.S. Tuley, R.J. Nicholas, Band gap dependent thermophotovoltaic device performance using the InGaAs and InGaAsP material system, *J. Appl. Phys.* 108 (2010), 084516.
- [14] G.D. Cody, Theoretical Maximum Efficiencies for Thermophotovoltaic Devices, 4th NREL Conf. Thermophotovoltaic Generation of Electricity, Denver, CO, 1998.
- [15] T.J. Coutts, J.S. Ward, Thermophotovoltaic and photovoltaic conversion at high-flux densities, *IEEE Trans. Electron. Dev.* 46 (1999) 2145.
- [16] J.L. Pan, H.K.H. Choy, C.G. Fonstad, Very large radiative transfer over small distances from a black body for thermophotovoltaic applications, *IEEE Trans. Electron. Dev.* 47 (2000) 241.
- [17] W.R. Chan, P. Bermel, R.C.N. Pilawa-Podgurski, C.H. Marton, K.F. Jensen, J. Senkevich, J.D. Joannopoulos, M. Soljačić, I. Celanovic, Toward high-energy-density, high-efficiency, and moderate-temperature chip-scale thermophotovoltaics, *Proc. Natl. Acad. Sci. U.S.A.* 110 (2013) 5309.
- [18] A. Fiorino, L. Zhu, D. Thompson, R. Mittapally, P. Reddy, E. Meyhofer, Nanogap near-field thermophotovoltaics, *Nat. Nanotechnol.* 13 (2018) 806–811.
- [19] C. Lucchesi, D. Cakiroglu, J. Perez, T. Taliercio, E. Tournié, P. Chapuis, R. Vaillon, Near-field thermophotovoltaic conversion with high electrical power density and cell efficiency above 14%, *Nano Lett.* 21 (2021) 4524–4529.
- [20] O.V. Sulima, A.W. Bett, M.G. Mauk, F. Dimroth, P.S. Dutta, R.L. Mueller, GaSb-, InGaAsSb-, InGaSb-, InAsSbP-and Ge-TPV cells for low-temperature TPV applications, *AIP Conf. Proc.* 653 (2003) 434.
- [21] V. Andreev, V. Khvostikov, O. Khvostikova, N. Kaluzhnii, E. Oliva, V. Rumyantsev, S. Titkov, M. Shvarts, Low-bandgap PV and thermophotovoltaic cells, in: *Proc. 3rd World Conf. on Photovoltaic Solar Energy* 15–18, 2003.
- [22] M.G. Mauk, O.V. Sulima, J.A. Cox, R.L. Mueller, Low-bandgap (0.3 to 0.5 eV) InAsSbP thermophotovoltaics, in: *3rd World Conf. on Photovoltaic Solar Energy*, 2003, p. 224.

- [23] K. Cheetham, P. Carrington, N. Cook, A. Krier, Low bandgap GaInAsSbP pentanary thermophotovoltaic diodes, *Sol. Energy Mater. Sol. Cell.* 95 (2011) 534–537.
- [24] A. Krier, M. Yin, A.R.J. Marshall, M. Kesaria, S.E. Krier, S. McDougall, W. Meredith, A.D. Johnson, J. Inskip, A. Scholes, Low bandgap mid-infrared thermophotovoltaic arrays based on InAs, *Infrared Phys. Technol.* 73 (2015) 126–129.
- [25] Q. Lu, X. Zhou, A. Krysa, A. Marshall, P. Carrington, C.-H. Tan, A. Krier, InAs thermophotovoltaic cells with high quantum efficiency for waste heat recovery applications below 1000°C, *Sol. Energy Mater. Sol. Cells* 179 (2018) 334–338. Q. Lu, private communication (2021).
- [26] D. Cakiroglu, J.-P. Perez, A. Evirgen, C. Lucchesi, P.-O. Chapuis, T. Taliercio, E. Tournié, R. Vaillón, Indium antimonide photovoltaic cells for near-field thermophotovoltaics, *Sol. Energy Mater. Sol. Cells* 203 (2019), 110190.
- [27] R.R. King, D. Bhusari, A. Boca, D. Larabee, X.-Q. Liu, W. Hong, C.M. Fetzer, D. C. Law, N.H. Karam, Band gap-voltage offset and energy production in next-generation multijunction solar cells, *Prog. in Photovoltaics* 19 (2011) 787.
- [28] M.G. Mauk, Z.A. Shellenbarger, J.A. Cox, O.V. Sulima, A.W. Bett, R.L. Mueller, P. E. Sims, J.B. McNeely, L.C. DiNett, Liquid-phase epitaxy of low-bandgap III-V antimonides for thermophotovoltaic devices, *J. Cryst. Growth* 211 (2000) 189–193.
- [29] X. Li, C. Lou, X. Li, Y. Zhang, Z. Liu, B. Yin, Bi₂Te₃/Si thermophotovoltaic cells converting low-temperature radiation into electricity, *Phys. Rev. Applied* 13 (2020), 041002.
- [30] A. Datas, R. Vaillon, Thermophotovoltaic energy conversion, Chapter 11, in: A. Datas (Ed.), *Ultra-High Temperature Thermal Energy Storage, Transfer and Conversion*, Woodhead Publishing, 2020, pp. 285–308.
- [31] Y. Wei, A. Hood, H. Yau, A. Gin, M. Razeghi, M.Z. Tidrow, V. Nathan, Uncooled operation of type-II InAs/GaSb superlattice photodiodes in the midwavelength infrared range, *Appl. Phys. Lett.* 86 (2005) 233106.
- [32] J.V. Li, C.J. Hill, J. Mumolo, S. Gunapala, S. Mou, S.-L. Chuang, Midinfrared type-II InAs/GaSb superlattice photodiodes toward room temperature operation, *Appl. Phys. Lett.* 93 (2008) 163505.
- [33] L. Lei, L. Li, H. Lotfi, H. Ye, R.Q. Yang, T.D. Mishima, M.B. Santos, M.B. Johnson, Mid-wavelength interband cascade infrared photodetectors with superlattice absorbers and gain, *Opt. Eng.* 57 (1) (2018), 011006.
- [34] W. Huang, L. Lei, L. Li, J.A. Massengale, R.Q. Yang, T.D. Mishima, M.B. Santos, Enhanced collection efficiencies and performance of interband cascade structures for narrow bandgap semiconductor thermophotovoltaic devices, *J. Appl. Phys.* 124 (2) (2018), 023101.
- [35] M.B. Reine, A.K. Sood, T.J. Tredwell, “Photovoltaic Infrared Detectors”, in: R. K. Willardson, A.C. Beer (Eds.), Chapter 6 in *Semiconductors and Semimetals*, vol. 18, Academic, New York, 1981, p. 201.
- [36] M.A. Green, Do built-in fields improve solar cell performance? *Prog. Photovoltaics Res. Appl.* 17 (2009) 57–66.
- [37] R.T. Hinkey, R.Q. Yang, Theory of multiple-stage interband photovoltaic devices and ultimate performance limit comparison of multiple-stage and single-stage interband infrared detectors, *J. Appl. Phys.* 114 (2013) 104506.
- [38] R.T. Hinkey, R.Q. Yang, Theoretical comparison of performance of limits of single- and multiple-stage photovoltaic devices, *Semicond. Sci. Technol.* 30 (2015), 015013.
- [39] W. Huang, R.Q. Yang, Limiting factors and efficiencies of narrow bandgap single-absorber and multi-stage interband cascade thermophotovoltaic cells under monochromatic light illumination, *J. Appl. Phys.* 126 (2019), 045714.
- [40] W. Huang, L. Li, L. Lei, Jeremy A. Massengale, H. Ye, Rui Q. Yang, Tetsuya D. Mishima, Michael B. Santos, Minority carrier lifetime in mid-wavelength interband cascade infrared photodetectors, *Appl. Phys. Lett.* 112 (2018) 251107.
- [41] R.Q. Yang, Infrared laser based on intersubband transitions in quantum wells, *Superlattice. Microsc.* 17 (1995) 77–83.
- [42] R.Q. Yang, Interband cascade (IC) lasers, in: A. Baranov, E. Tournie (Eds.), *Semiconductor Lasers: Fundamentals and Applications*, Woodhead Publishing, Oxford, UK, 2013, Chap. 12.
- [43] I. Vurgaftman, R. Weil, M. Kamp, J.R. Meyer, C.L. Canedy, C.S. Kim, M. Kim, W. W. Bewley, C.D. Merritt, J. Abell, S. Höfling, Interband cascade lasers, *J. Phys. D Appl. Phys.* 48 (2015) 123001.
- [44] R.Q. Yang, L. Li, W. Huang, S.M.S. Rassel, J.A. Gupta, A. Bezinger, X. Wu, S. G. Razavipour, G.C. Aers, InAs-based interband cascade lasers, *IEEE J. Sel. Top. Quant. Electron.* 25 (6) (2019), 1200108.
- [45] J.R. Meyer, W.W. Bewley, C.L. Canedy, C.S. Kim, M. Kim, C.D. Merritt, I. Vurgaftman, The interband cascade laser, *Photonics* 7 (2020) 75.
- [46] G.A. Sai-Halasz, R. Tsu, L. Esaki, A new semiconductor superlattice, *Appl. Phys. Lett.* 30 (1977) 651.
- [47] G.A. Sai-Halasz, L.L. Chang, J.-M. Welter, C.A. Chang, L. Esaki, Optical absorption of In_{1-x}Ga_xAs-GaSb_yAs_z superlattices, *Solid State Commun.* 27 (1978) 935.
- [48] L. Esaki, L.L. Chang, E.E. Mendez, Polytype superlattices and multi-heterojunctions, *Jpn. J. Appl. Phys.* 20 (1981) LS29.
- [49] H. Lotfi, L. Li, H. Ye, R.T. Hinkey, L. Lei, R.Q. Yang, J.C. Keay, T.D. Mishima, M. B. Santos, M.B. Johnson, Interband cascade infrared photodetectors with long and very-long cutoff wavelengths, *Infrared Phys. Technol.* 70 (2015) 162–167.
- [50] D. Zhang, E. Dupont, R.Q. Yang, H.C. Liu, C.-H. Lin, M. Buchanan, S.S. Pei, Long-wavelength infrared (~10–15 μm) electroluminescence from Sb-based interband cascade devices, *Opt Express* 1 (1997) 97.
- [51] R.Q. Yang, Z. Tian, J. Klem, T.D. Mishima, M.B. Santos, M.B. Johnson, Interband cascade photovoltaic devices, *Appl. Phys. Lett.* 96 (2010), 063504.
- [52] R.T. Hinkey, Z. Tian, S.M. Rassel, R.Q. Yang, J.F. Klem, M.B. Johnson, Interband cascade photovoltaic devices for conversion of mid-infrared radiation, *IEEE J. Photovoltaics* 3 (2013) 745.
- [53] H. Lotfi, R.T. Hinkey, L. Li, R.Q. Yang, L. Lei, M.B. Johnson, T.D. Mishima, M. B. Santos, Narrow-bandgap photovoltaic devices operating at room temperature and above with high open-circuit voltage, *Appl. Phys. Lett.* 102 (2013), 211103.
- [54] H. Ye, H. Lotfi, L. Li, R.T. Hinkey, R.Q. Yang, L. Lei, J.C. Keay, M.B. Johnson, T. D. Mishima, M.B. Santos, Multi-stage interband cascade photovoltaic devices with a bandgap of 0.23 eV operating above room temperature, *Chin. Sci. Bull.* 59 (10) (2014) 950–955.
- [55] R.Q. Yang, H. Lotfi, L. Li, R.T. Hinkey, H. Ye, J.F. Klem, L. Lei, T.D. Mishima, J. C. Keay, M.B. Santos, Quantum-engineered interband cascade photovoltaic devices, *Proc. SPIE* 8993 (2014), 899310.
- [56] H. Lotfi, R.T. Hinkey, L. Li, R.Q. Yang, J.F. Klem, J.C. Keay, M.B. Johnson, Multi-stage photovoltaic devices with a cutoff wavelength of ~3 μm, in: *Proc. of the 40th IEEE Photovoltaic Specialists Conference*, 2014, pp. 220–223.
- [57] H. Lotfi, L. Li, L. Lei, R.Q. Yang, J.F. Klem, M.B. Johnson, Narrow-bandgap interband cascade thermophotovoltaic cells, *IEEE J. Photovoltaics* 7 (2017) 1462.
- [58] W. Huang, L. Li, J.A. Massengale, R.Q. Yang, T.D. Mishima, M.B. Santos, Investigation of narrow bandgap interband cascade thermophotovoltaic cells, *Proc. SPIE* 10913 (2019), 1091317.
- [59] W. Huang, J.A. Massengale, Y. Lin, L. Li, R.Q. Yang, T.D. Mishima, M.B. Santos, Performance analysis of narrow-bandgap interband cascade thermophotovoltaic cells, *J. Phys. D* 53 (17) (2020), 175104.
- [60] R.Q. Yang, J.M. Xu, Bound and quasibound states in leaky quantum wells, *Phys. Rev. B* 46 (1992) 6969.
- [61] R.Q. Yang, J.M. Xu, Leaky quantum wells: a basic theory and application, *Can. J. Phys.* 70 (1992) 1153.
- [62] R.Q. Yang, Z. Tian, Z. Cai, J.F. Klem, M.B. Johnson, H.C. Liu, Interband cascade infrared photodetectors with superlattice absorbers, *J. Appl. Phys.* 107 (5) (2010), 054514.
- [63] Z. Tian, R.Q. Yang, T.D. Mishima, M.B. Santos, Plasmon-waveguide interband cascade lasers near 7.5 μm, *Photonics Technol. Lett.* 21 (2009) 1588.
- [64] J.R. Meyer, C.A. Hoffman, F.J. Bartoli, L.R. Ram-Mohan, Type-II quantum-well lasers for the mid-wavelength infrared, *Appl. Phys. Lett.* 67 (1995) 757.
- [65] H. Lotfi, L. Li, S.M.S. Rassel, R.Q. Yang, C.J. Corrège, M.B. Johnson, P.R. Larson, J. A. Gupta, Monolithically integrated mid-IR interband cascade laser and photodetector operating at room temperature, *Appl. Phys. Lett.* 109 (2016), 151111.
- [66] S.S. Hegedus, Current-voltage analysis of a-Si and a-SiGe solar cells including voltage-dependent photocurrent collection, *Prog. Photovoltaics Res. Appl.* 5 (1997) 151–168.
- [67] J. Nelson, *The Physics of Solar Cells*, Imperial College Press, London, UK, 2003.
- [68] S. Hegedus, D. Desai, C. Thompson, Voltage dependent photocurrent collection in CdTe/CdS solar cells, *Prog. Photovoltaics Res. Appl.* 15 (2017) 587–602.
- [69] J. Phillips, J. Titus, D. Hoffman, Determining the voltage dependence of the light generated current in CuInSe₂-based solar cells using I-V measurements made at different light intensities, in: *Proceedings of 26th IEEE Photovoltaic Specialists Conference*, 1997, pp. 463–466.
- [70] W. Huang, L. Li, L. Lei, Jeremy A. Massengale, H. Ye, Rui Q. Yang, Tetsuya D. Mishima, Michael B. Santos, Minority carrier lifetime in mid-wavelength interband cascade infrared photodetectors, *Appl. Phys. Lett.* 112 (2018), 251107.
- [71] W. Huang, J.A. Massengale, Y. Lin, R.Q. Yang, T.D. Mishima, M.B. Santos, Resonant cavity enhanced interband cascade thermophotovoltaic cells, in: *Proc. Of 2020 IEEE Photovoltaics Specialists Conference*, 2020, pp. 825–828.
- [72] W. Huang, R.Q. Yang, Conversion efficiency of resonant cavity enhanced narrow bandgap interband cascade photovoltaic cells, *J. Appl. Phys.* 128 (2020), 214502.
- [73] E. Yablonovitch, Statistical ray optics, *J. Opt. Soc. Am. A* 72 (1982) 899.
- [74] D.M. Callahan, J.N. Munday, H.A. Atwater, Solar cell light trapping beyond the ray optic limit, *Nano Lett.* 12 (2012) 214.
- [75] A.G. Dentai, R. Kuchibhotla, J.C. Campbell, C. Tsai, C. Lei, High quantum efficiency, long wavelength InP/InGaAs microcavity photodiode, *Electron. Lett.* 27 (1991) 2125.
- [76] M.S. Ünlü, S. Strite, Resonant cavity enhanced photonic devices, *J. Appl. Phys.* 78 (1995) 607.
- [77] C.L. Canedy, W.W. Bewley, C.D. Merritt, C.S. Kim, M. Kim, M.V. Warren, E. M. Jackson, J.A. Nolde, C.A. Affouda, E.H. Aifer, I. Vurgaftman, J.R. Meyer, Resonant-cavity infrared detector with five-quantum-well Absorber and 34% external quantum efficiency at 4 μm, *Opt Express* 27 (2019) 3771.
- [78] F.Y. Huang, A. Salvador, X. Gui, N. Teraguchi, H. Morkoc, Resonant-cavity GaAs/InGaAs/AlAs photodiodes with a periodic absorber structure, *Appl. Phys. Lett.* 63 (1993) 141.
- [79] W.W. Bewley, C.L. Canedy, M.V. Warren, C.S. Kim, C.D. Merritt, I. Vurgaftman, J. R. Meyer, M. Kim, Room-temperature mid-infrared interband cascade vertical-cavity surface-emitting laser, *Appl. Phys. Lett.* 99 (2016), 151108.
- [80] V. Jayaraman, B. Kolasa, C. Lindblad, A. Cazabat, C. Burgner, S. Segal, K. Lascola, F. Towner, F. Xie, Tunable room-temperature continuous-wave mid-infrared VCSELs, *Proc. SPIE* 11300 (2020), 11300M.
- [81] J. Yin, R. Paiella, Multiple-junction quantum cascade photodetectors for thermophotovoltaic energy conversion, *Opt Express* 18 (2010) 1618.
- [82] J. Yin, R. Paiella, Limiting performance analysis of cascaded interband/intersubband thermophotovoltaic devices, *Appl. Phys. Lett.* 98 (2011), 041103.
- [83] W. Huang, S.M. Shazzad Rassel, L. Li, J.A. Massengale, R.Q. Yang, T.D. Mishima, M.B. Santos, A unified figure of merit for interband and intersubband cascade devices, *Infrared Phys. Technol.* 96 (2019) 298.
- [84] D.Z.-Y. Ting, A. Soibel, L. Hoglund, J. Nguyen, C.J. Hill, A. Khoshakhlagh, S. D. Gunapala, “Type-II superlattice infrared detectors”, in: S.D. Gunapala, D. R. Rhiger, C. Jagadish (Eds.), Chapter 1 in *Semiconductors and Semimetals* vol. 84, 2011.

- [85] A. Rogalski, P. Martyniuk, M. Kopytko, Type-II superlattice photodetectors versus HgCdTe photodiodes, Proc. SPIE 11151 (2019), 1115114.
- [86] E.H. Steenbergen, G. Ariyawansa, C.J. Reyner, G.D. Jenkins, C.P. Morath, J. M. Duran, J.E. Scheibling, V.M. Cowan, A recent review of mid-wavelength infrared type-II superlattices: carrier localization, device performance, and radiation tolerance, Proc. SPIE 10111 (2017), 1011104.
- [87] E.H. Steenbergen, B.C. Connelly, G.D. Metcalfe, H. Shen, M. Wraback, D. Lubyshev, Y. Qiu, J.M. Fastenau, A.W.K. Liu, S. Elhamri, et al., Significantly improved minority carrier lifetime observed in a long-wavelength infrared III-V type-II superlattice comprised of InAs/InAsSb, Appl. Phys. Lett. 99 (2011), 251110.
- [88] B.V. Olson, E.a. Shaner, J.K. Kim, J.F. Klem, S.D. Hawkins, L.M. Murray, J. P. Prineas, M.E. Flatte, T.F. Boggess, Time-resolved optical measurements of minority carrier recombination in a mid-wave infrared InAsSb alloy and InAs/InAsSb superlattice, Appl. Phys. Lett. 101 (2012), 092109.
- [89] L. Lei, L. Li, H. Lotfi, Y. Jiang, R.Q. Yang, M.B. Johnson, D. Lubyshev, Y. Qiu, J. M. Fastenau, A.W.K. Liu, Mid-wave interband cascade infrared photodetectors based on GaInAsSb absorbers, Semicond. Sci. Technol. 31 (2016) 105014.
- [90] L. Shterengas, G. Kipshidze, T. Hosoda, R. Liang, T. Feng, M. Wang, A. Stein, G. Belenky, Cascade pumping of 1.9–3.3 μm type-I quantum well GaSb-based diode lasers, IEEE J. Sel. Top. Quant. Electron. 23 (6) (2017) 1500708.
- [91] L. Li, H. Ye, Y. Jiang, R.Q. Yang, J.C. Keay, T.D. Mishima, M.B. Santos, M. B. Johnson, MBE-grown long-wavelength interband cascade lasers on InAs substrates, J. Cryst. Growth 425 (2015) 369–372.